DEVELOPMENT OF A METHOD FOR DETERMINING TENSILE STRENGTH OF ALGAL FILAMENTS USING MOTION CAPTURE

By

Andrés Felipe Alzate

May 2013

A thesis submitted to the
Faculty of the Graduate School of
the University at Buffalo, State University of New York
in partial fulfillment of the requirements for the
degree of

Master of Science

Department of Civil, Structural, and Environmental Engineering

Acknowledgments

I would first like to formally thank my main advisor Dr. David M. Blersch, for his dedication to providing constructive feedback and the many insightful talks which brought about the fruitful research questions explored in this thesis and future research plans. Thank you for your time and patience in helping my often abstract and unorthodox methods, to be driven down to a viable and attainable research contribution.

I would also like to thank Dr. Joseph F. Atkinson and Dr. James N. Jensen for their valuable comments and feedback during the course of my academic career. Their lessons have heightened my respect for various subjects such as biology, fluid mechanics, and mathematics through their insightful and innovative teaching methods and insight outside of the classroom. I would also like to give thanks to the rest of the superb faculty at the University at Buffalo who have not only granted their time and energy to ensure I leave the University with an important set of skills but have also provided moral support during the rough patches along the way.

I will also give many thanks to my friends and classmates who have provided help and support during this academic journey. Those long studious nights seemed bearable as long as there was companionship to share and divide the heavy burden. In particular, I would like to thank Juan H. Aleman for providing insight into the field of structural dynamics to help provide the last missing piece to this particular research endeavor.

Last but not least, I would like to thank my parents, who have continuously been there to provide support and motivation. I ultimately dedicate this thesis to my parents Gildardo and Luz Marina Alzate, as they provided me the opportunity to obtain an education that that they never had a chance to receive.

Table of Contents

Table of Figures

Table of Tables

Abstract

One of the most difficult endeavors in filamentous algal growth models is predicting the occurrence of sloughing. Algal sloughing can stem from various sources such as from biological or mechanical means. The focus of this study is to investigate the role of fluid shear on the benthic filament mass. This research proposes a method to model the external forces on a benthic filament from the aquatic environment and the internal forces from the movement of the filament mass itself. To accomplish this, three parallel endeavors were pursued. First, a fluid-structure force interaction model was developed that can be applied to a multi-node cylindrical benthic filament model. Second, a finite element modeling approach was used to estimate the internal structural properties based on the filament mass displacement under a specified external force. Third, motion capture techniques from experimental video footage were utilized to provide data for the fluid-structure interaction model and validation of the finite-element model. In laboratory application of this methodology on an experimental sample of mixed-culture filamentous algae, a value of 4.2 MPa was calculated for the internal stress in a filament, a value in close agreement with literature values. This method can provide an in-situ approach to investigate the structural properties of the algal filament in its natural aquatic environment without the use of expensive equipment.

1.0: Introduction

Algal filament biomass can be thought of as both a valued commodity and a municipal problem. Algae can be used as a viable protein additive to products such as cattle-feed (Wullepit, Hostens et al. 2012) or for its lipid content for bio-fuel production (Adey, Kangas et al. 2011). The filamentous algae production process could even serve as a viable service such as a phytoremediation application (Kuritz and Wolk 1995) to remove nutrient contaminants from an incoming stream (Adey and Loveland 2007). Alternately, decaying filamentous algae can be seen as a public nuisance in natural bodies of water (Parker and Maberly 2000), and actions are often taken to limit or avoid sudden proliferation of algal blooms that can result in lowering of dissolved oxygen content due to excessive organic detritus (Depew, Houben et al. 2011).

The excessive growth of benthic filamentous algae in nutrient-loaded aquatic environments often leads to poor water quality and nuisance conditions from excessive algal biomass accumulation (Hamilton, McVinish et al. 2009). A key component of understanding the accumulation and transport of benthic filamentous biomass is the modeling of the initiation of sloughing events, where weakening and breakage of algal filaments causes loss of active growing biomass (Poff, Voelz et al. 1990). Sloughing occurs typically through the intersection of internal biological growth conditions, affected by external limitations of nutrients or light, with external force application from flowing or circulating water (Hart and Finelli 1999). Because of difficulty in measurement, little is known about the precise intensity of internal stress within the algal filament biomass that results in breakage (Johnson, Shivkumar et al. 1996). There is a need, therefore, for the development of a method for determining the ultimate stress within a benthic algal filament for use in refining models of growth and transport of benthic algae in both natural and cultivation scenarios.

1.1: Objectives and Tasks

The primary objective of this study was to develop a method to investigate the influence of fluid forces acting upon the algal filament structure. To refine the current algal sloughing models, an analytical model was developed that integrates the idea of modeling the benthic algal filament as a cylindrical structure with structural dynamics to determine internal filament stresses that can contribute to breakage and mass sloughing. To accomplish this, a parallel series of tasks were undertaken:

- A fluid-structure force interaction model was developed that can predict the force on a particular point on a theoretical algal filament which can bend on multiple hinged joints.

- A finite element structural model was developed that can accurately describe how the structural filament might move and resist external force to back calculate the material properties of the algal filament.

- Motion capture techniques were utilized in an algal filament flume experiment to provide data to calibrate the coupled fluid force and benthic structure models.

The first task was to develop a model that can predict the amount of force applied on a specific region of the algal filament. The model should be flexible enough to encompass the dynamically changing geometry of an algal filament moving on multiple joints. The model must also include forces derived from different physical sources such as the physical geometry of the algal filament and the spatially dependent fluid force from the aquatic environment.

The second task was to model the effect of the applied force on the algal filament movement. The velocity of the algal filament, given a known applied force, can provide an

estimation of the structural resistance within the filament. Under the same applied load, an algal filament with a high structural stiffness would not move very much. An algal filament with a low structural strength would move a great distance and have the properties of a weak cable. Two types of data would be needed for model calibration: the force applied on the algal structure and a measure of algal motion after that force was applied.

The third task is to acquire the spatial data of the algal filament which will feed into both models. The applied force model will utilize the spatial data set to know the position and configuration of the algal filament over time to calculate the magnitude of the net force in a specific area on the algal filament. Since the applied force is dependent on how the algal filament is arranged to the oncoming flow, a method of machine vision was implemented to record the spatial arrangement of the benthic filament. The spatial data are also crucial to the structural model because the time-referenced position of the algal filament can provide reference to gauge the accuracy of the model.

2.0: Background

One of the first studies applied a force balance emphasizing the effects of the stream environment on a periphyton filament (Nikora, Goring et al. 1998). This idea was further extended by investigating the stresses on the algal filament in a more controlled flume environment to investigate the mechanistic shearing (Hondzo and Wang 2002). By developing these methods further, future research can be conducted to investigate the structural properties of an algal filament in a stream flow environment.

2.1.0: Development of the exerted Fluid-Force Model

Modeling the sloughing of benthic algal filaments in a fluid flow environment requires the development of a model representing the interaction of the induced forces from the flow field and the physical representation of the algal filament. First, a representation of the fluid flow environment is developed through the representation of the distribution of velocities through the depth of the flowing fluid. Next, the geometric representation of the algal filament is developed. Finally, based on these representations, the general force balance on the generalized element of the algal filament is developed in two coordinate directions.

2.1.1: Logarithmic Velocity Profile Modeling

To understand the effects of fluid mechanics on a particular system, it is necessary to first have a working knowledge of some basic principles associated with fluid flow. One case to investigate would be the flow of water past an infinitely flat plate. If the fluid did not experience viscosity across the flat plate, then a uniform velocity profile could be assumed as seen in (a) of Figure 1. Assuming a zero slip condition, where the fluid meets the plate, the velocity of the fluid is zero at the plate and the velocity decreases further away from the plate as seen in (b) of Figure 1 (Young 2007).

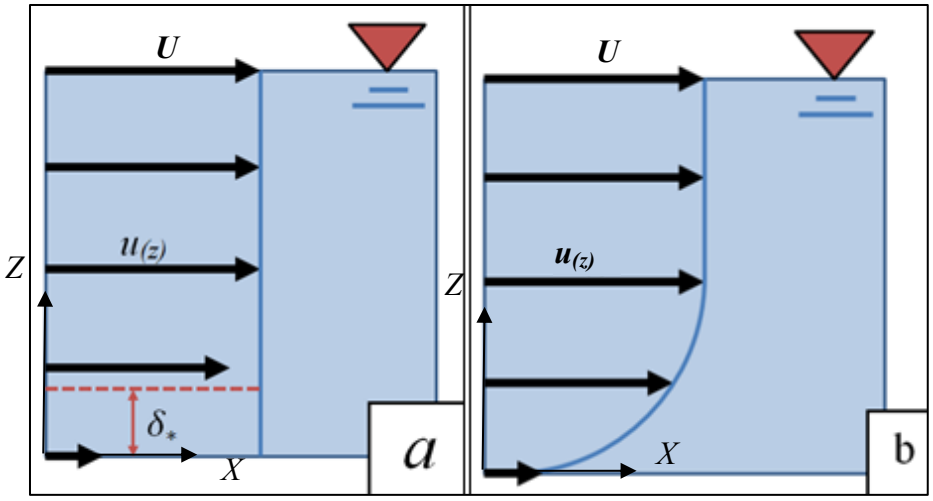

Figure 1: (a) Uniform velocity profile (b) Logarithmic velocity profile.

The vertical velocity can thus be represented by a logarithmic function in equation (1).

$$\bar{U}_{(z)} = \frac{U_*}{\kappa} \ln\left(\frac{Z}{Z_0}\right) \qquad (1)$$

where $\bar{U}_{(z)}$ is the local mean velocity as a function of vertical height [m/s] (Rubin and Atkinson 2001), U_* is the friction velocity [m/s] (Rubin and Atkinson 2001), κ is the universal von Karman constant (~0.41) [dimensionless] (Xu, Wright et al. 1994), Z is the vertical distance from the plate surface [m], and Z_0 is the roughness length [m] (Rubin and Atkinson 2001).

It can be assumed that the friction velocity (U_*) is 1/10 the specific discharge (Rubin and Atkinson 2001) which can be determined using equation (2) (Rubin and Atkinson 2001).

$$q = \frac{Q}{A_{cross}} \qquad (2)$$

where q represents the specific discharge which is the volumetric discharge per cross sectional area [m/s], Q represents the volumetric flow rate [m^3/s], and A_{cross} is the cross sectional area of the open channel flow [m^2].

Assuming that the surface over which the fluid flows is a flat and smooth flume floor, the roughness length coefficient can be modeled using equation (3) (Nikora, Goring et al. 1998).

$$Z_0 = b\frac{\nu}{U_*} \qquad (3)$$

where b is a unit less parameter in the range of 0.11-0.13 (Gibson 1972), and U is the average velocity of water [m/s], and ν is the kinematic viscosity of water [m^2/s].

2.1.2: Algal Filament Bundle Model Development

To investigate the direct effects of fluid flow on an algal filament bundle, a force balance approach can be taken to estimate the structural properties. Even though the algal filament bundle has a very complex shape that might be simulated numerically (Bruss and Grason 2012), a simplified geometric representation is useful for a force balance. A cylindrical shape has been widely used in structural applications to model a complex intertwined fibrous cable (Lan and Shabana 2010), a useful form for representing a bundle of algal filaments The benthic filament has been treated in the past, as a single rigid cylindrical structure that can pivot only at the basal attachment point as a result of induced forces from oncoming flow (Denny and Hale 2003). The representation of the algal filament bundle as a straight, single-hinged cylinder is an approach for algal filament bundle modeling (Hondzo and Wang 2002). In reality, however, the cylinder is not completely straight, as it is usually curved and oscillates within the overlying flow.

Therefore, the representation of the algal filament as a series of interconnected rigid cylinders that pivot on hinged connection points is closer to what is actually observed, which can be seen in Figure 2. This suggests an approach of using multiple sections and applying equations of motion at each (Denny and Hale 2003).

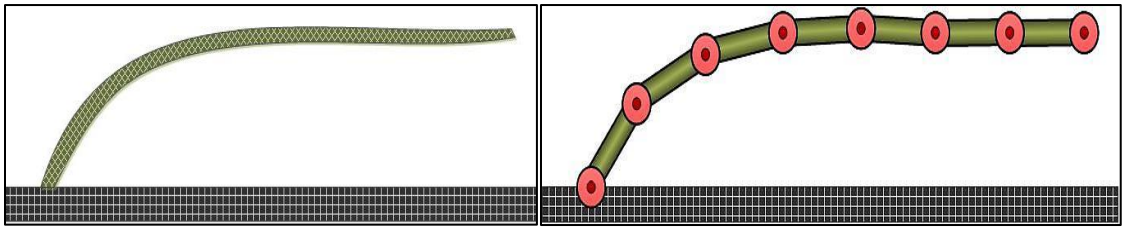

Figure 2: Algal filament bundle (left) and hinged cylinder model in straightened flow (right).

The algal filament bundle can be broken up into interconnected cylindrical sections, as in Figure 3, where N_i represents the connection points, or nodes, and L_i represents the section, or link, between the nodes. This approach results in a system that exhibits temporal and spatial variation. To keep the elements well referenced, the individual links can be referenced in terms of the subscript k and the individual segment nodes are referenced as j in Figure 3.

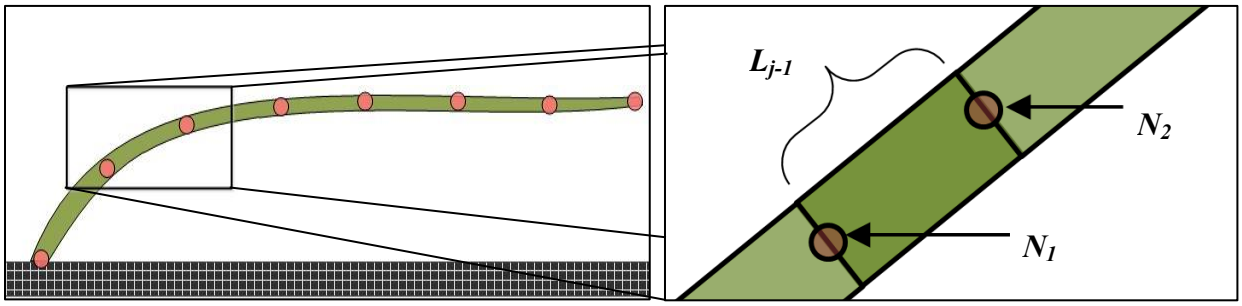

Figure 3: Broad and close up view of the node and link labeling scheme.

The position of each individual benthic filament bundle link changes with time and will be assumed to move only within a two dimensional Cartesian plane, defined by x and z

coordinates (Figure 6). To label the time-referenced values, the subscript *i* will be used and the individual nodes can be completely labeled as seen in Figure 4. Although a true fluid velocity system can act in three dimensions, an attempt will be made to ensure a three dimensional system can be treated as a two dimensional system for simplicity. One way this can be modeled physically is by placing the benthic filament bundle in the middle of a straightened flow channel.

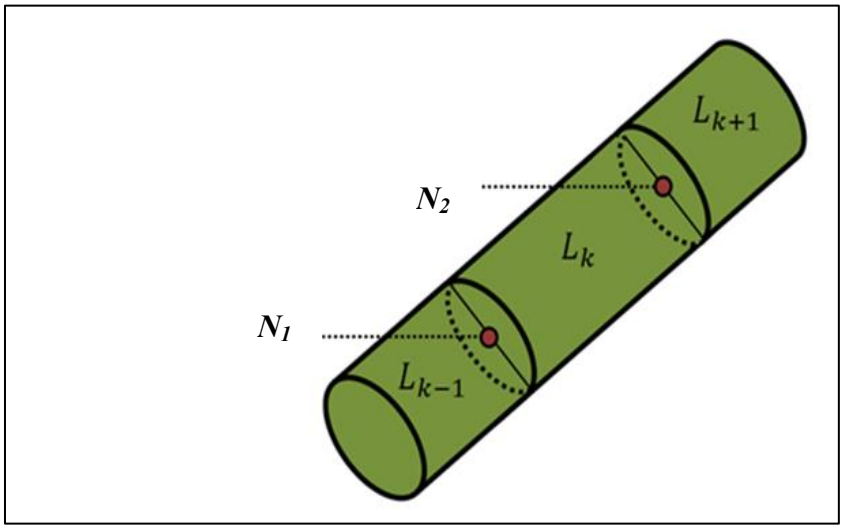

Figure 4: Three-dimensional spatial and temporal labeling scheme for an algal filament.

As the simplified segmented algal filament bundle bends, each paired set of nodes provides an orientation angle θ_k of the link L_k with the direction of oncoming flow (Figure 5). Treating each separate filament bundle between nodes as a cylinder oriented in space at an angle can provide a more detailed description of the magnitude of the force felt in that particular link section of the algal filament bundle. The orientation of this cylinder is important because there are variations in pressure distribution along its length giving rise to differences in drag and lift forces.

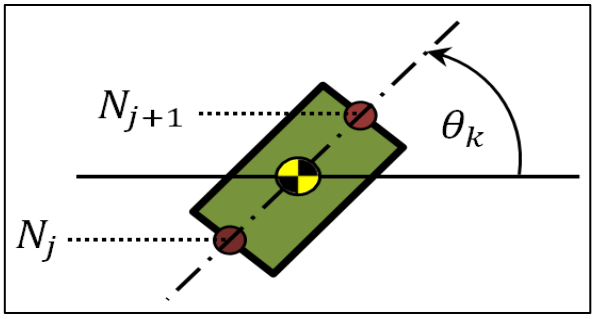

Figure 5: Algal filament bundle link orientation angle schematic.

2.1.3: Horizontal Force Model on a Benthic Filament Bundle

The first objective was to create a force model that can predict how much force is experienced on a particular point on the algal filament bundle. Taking a force balance on a straight rigid cylinder with one hinge, it can be assumed that there are eight types of forces at work, as can be seen in Figure 6.

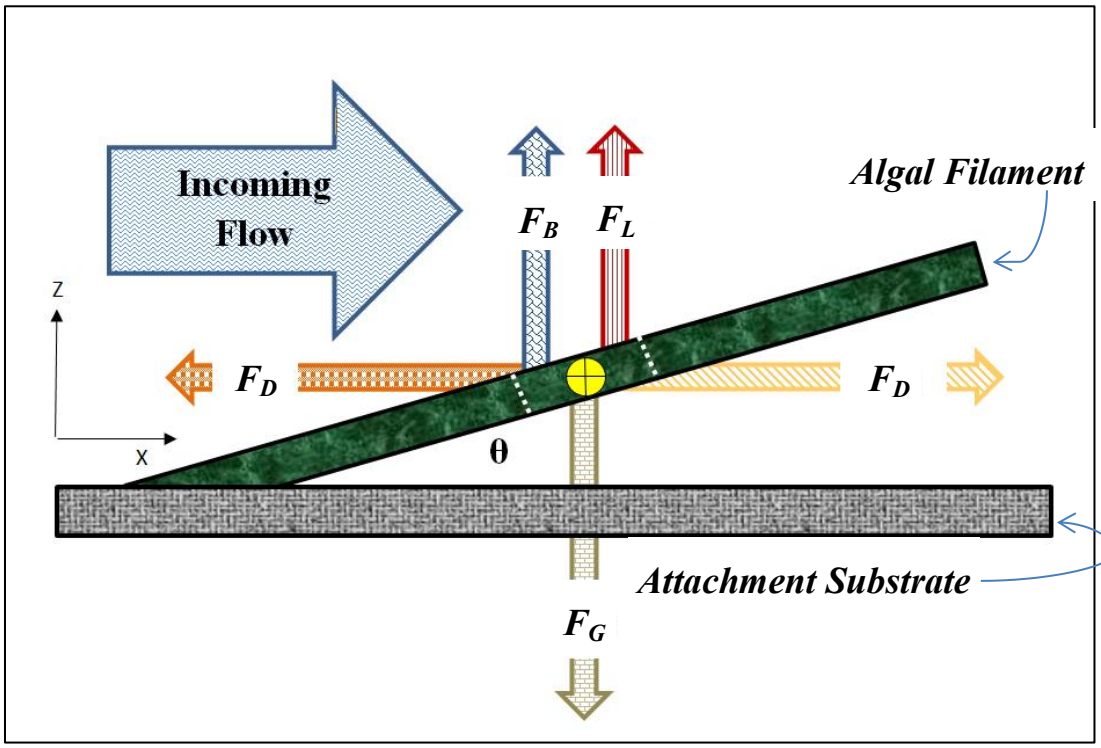

Figure 6: Single hinged algal filament bundle model schematic.

The eight types of external forces acting directly on the algal filament bundle include the internal tensile stress (F_C), buoyancy force (F_B), hydrodynamic lift force (F_L), fluid drag force (F_D), and the force of gravity (F_G). The external forces place an opposing force upon the internal tensile stress (F_C) which acts in the axial direction of the benthic filament bundle. Figure 6 depicts an algal filament bending at an angle θ with the stress decomposed into its vertical $\left(F_{C_z}\right)$ and horizontal $\left(F_{C_x}\right)$ components.

Based on Figure 6, the only fluid forces that act in the horizontal direction are the fluid drag force and the horizontal component of the tensile strength of the algal filament bundle. The opposing algal filament bundle horizontal force ($F_{C,x}$) will be independently calculated in the finite element model that will be presented in Chapter 2.2.3. The finite element structural model computes values of the opposing tensile force using the values of fluid drag as the imposed force on a given algal node on an algal filament bundle. The fluid drag force can be modeled using equation (4) (Young 2007).

$$F_D = \frac{\rho}{2}[A_D(\Delta Z, \phi)][C_D(Re)][U_*^2] \qquad (4)$$

where F_D is the force on the algal filament bundle due to fluid drag [N] (Hondzo and Wang 2002), ρ is the fluid density [kg/m^3], $A_D(\Delta Z, \phi)$ the projected area perpendicular to the oncoming flow [m^2] (see Figure 7 for clarification), $C_D(Re)$ is the drag force coefficient which is a function of the Reynolds number [dimensionless].

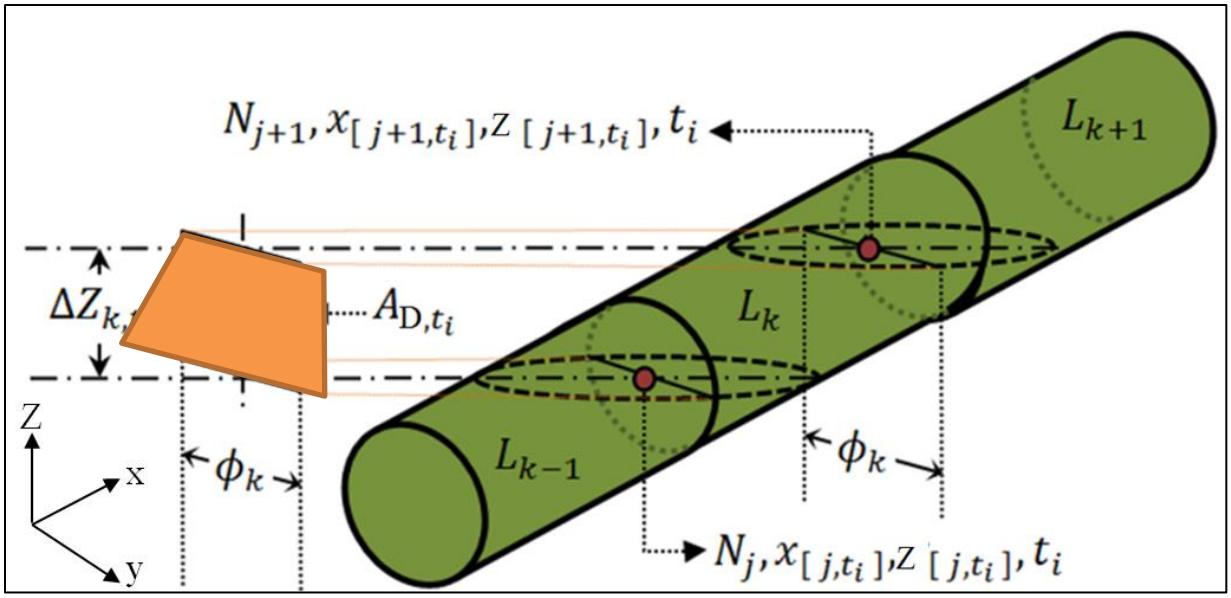

Figure 7: Geometric drag area $A_{D,ti}$ between two algal filament bundle nodes.

The position of the algal filament nodes are labeled as "*N*" which are spatially and temporally referenced on a two dimensional plane (*X, Z*). The projected area of the algal filament bundle onto the *Z, Y* plane corresponds to the drag area between these nodes.

Table 1: Table of symbol definitions for the numerical algal bundle filament link modeling.

Symbol	Ref. Subscript	Description
ϕ	k	Benthic filament diameter at specified node
L	k	Benthic filament link at specified
N	k	Benthic filament node reference
x	j, t_i	Horizontal distance of referenced node at a specific time
z	j, t_i	Vertical distance of referenced node at a specific time
t	i	Referenced time value

If many nodes were used, the link lengths would be relatively small, and a simple cylindrical application could be used. However, in this study the nodes were few and far apart to reduce computational complexity. To replicate the geometry of an algal filament bundle, a tapered cylinder approach was used and appropriate calculations were undertaken, as listed in Appendix A, section 4. The reason for using a tapered cylinder geometry in this study is that algal filament bundles are often much thicker at the attachment base and become progressively thinner as they extend further into the flow current (Astbury and Preston 1940).

The drag force area corresponds to the projected planar area of the algal filament bundle which is perpendicular to the flow direction. The drag area for a segment of filamentous algae in a straight fluid flow condition is a trapezoid whose base widths include the filament bundle diameter of the node of interest and the midpoint of the corresponding link (see Appendix A: section 2). The vertical length of the trapezoid is dependent on the vertical difference between the node of interest and the midpoint of the appropriate link. The drag area, which corresponds to an individual numerical node in the finite element model, utilizes the drag areas before and after the midpoints of the previous and subsequent link from the node of interest, as shown in Figure 8.

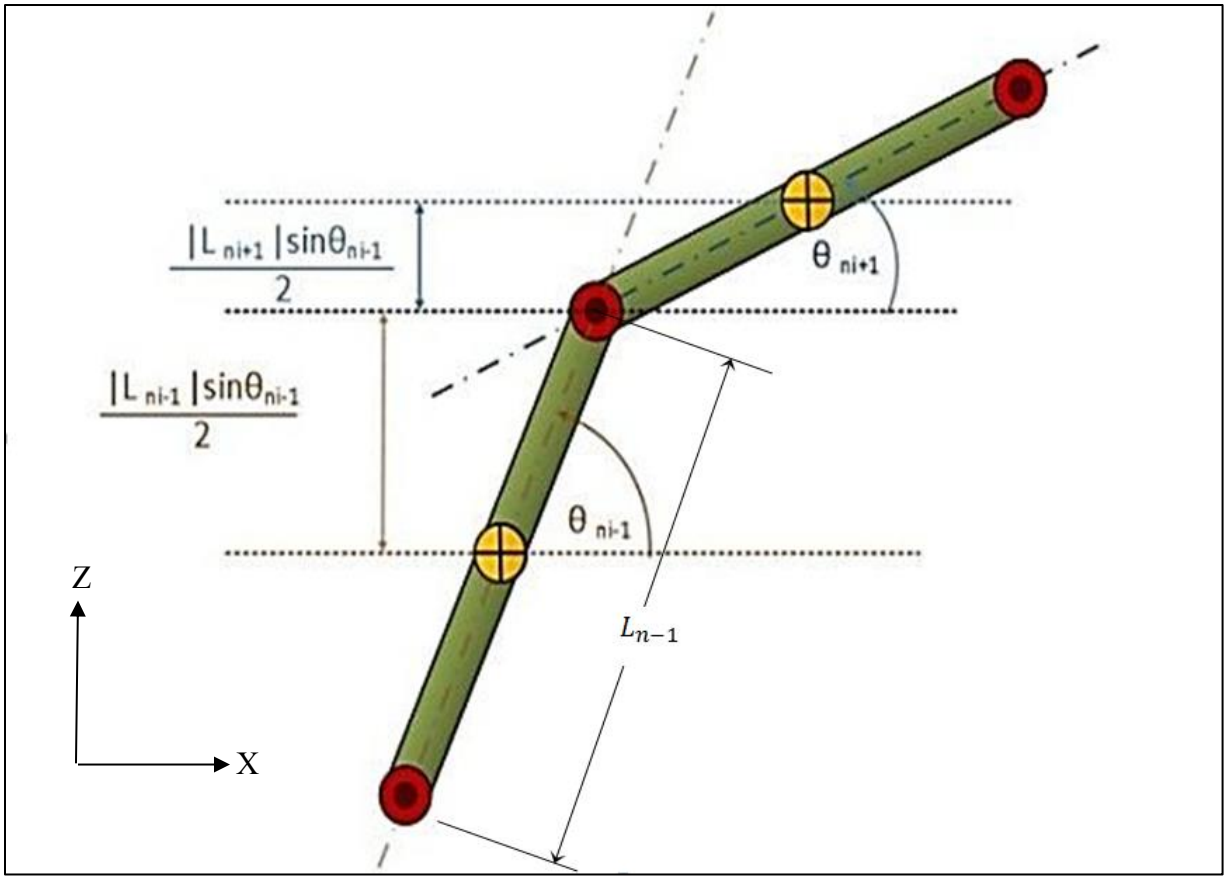

Figure 8: Numerical length dimension for drag area for individual node.

The drag force on a given node is calculated from the drag force from the midpoints of the links before and after the specified node. Therefore, two drag force calculations must be made for each node. The only exception to this rule must be made from the first and last node calculation, which requires calculating one drag force area that is before or after in each specific case. The drag force area for a tapered cylinder before a specific node n_j has been formally calculated in Appendix A: section 3 and the result can be seen in Equation (5).

$$A_{D\,j,t_i} = \left(\phi_i + \left(\frac{\phi_{i-1} - \phi_i}{4}\right)\right)\left(\frac{\left(z_{[j,t_i]} - z_{[j-1,t_i]}\right)}{2}\right) \qquad (5)$$

The drag area, which corresponds to a specific node in Figure 8, is ascribed to the middle node that utilizes spatial information from the previous and subsequent nodes to calculate the corresponding drag area. Thus, the middle node drag area is based on half of the perpendicular planar area of the benthic filament bundle links before and after the middle node. Therefore, the drag area for a given node corresponds to half of the drag area of the benthic filament bundles before and after. When the previous and consecutive nodes are above or below the specified node, there is an assumption that the drag force does not dissipate in energy as it flows around the first benthic link column and then progresses to the other.

The value for the overall drag force could be determined experimentally through a device such as a spring balance holding on to a benthic filament bundle in flow (Schutten and Davy 2000). The drag coefficient is often determined experimentally over a wide range of flow conditions which are often characterized by a flow classification parameter such as Reynolds number, the attributes of the object shape, and the orientation of the shape in relation to the oncoming flow (Young 2007). The various parameters present provide a drag force coefficient with a wide range. This coefficient could affect how much drag force is exerted on an object in flow.

The process of applying a statistical model from experimental data can be seen in Figure 9 (Young 2007). The results seem to take on the form of a power function. This function has a high degree of correlation and accuracy to the referenced figure to predict the drag coefficient behavior with the Reynolds number.

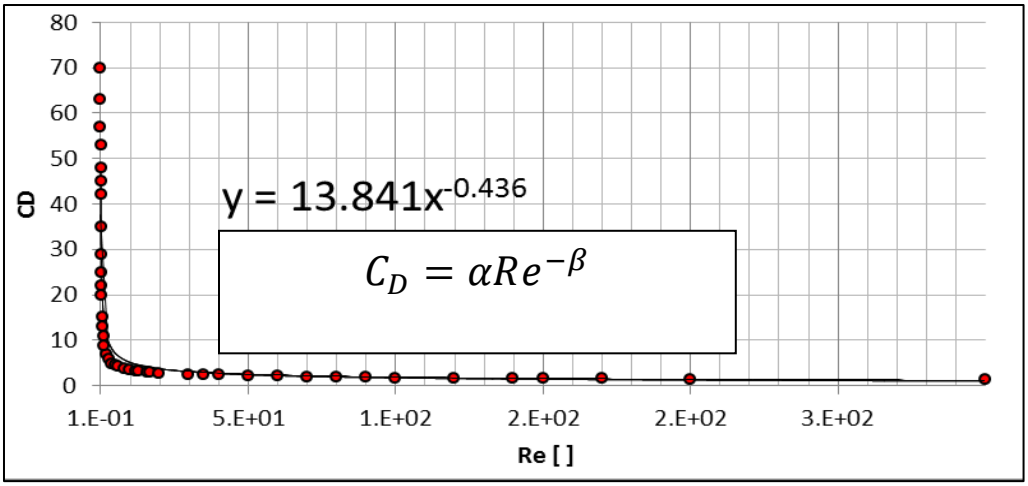

Figure 9: Drag coefficient (C_D) as a function of Reynolds number (Re) for flow over a smooth cylinder, based on data from Young (2007), p. 351.

2.1.4: Vertical Force Model on Benthic Filament Bundle

The forces in the vertical direction of an algal filament bundle comprise three distinct types of forces (Figure 10). The forces of gravity F_G and buoyancy F_B are dependent on the algal link geometry, while the lift force F_L is subject to the angle orientation of the link. There is a difference in complexity between two groups of equations because the buoyancy and gravitational forces remain constant due to the consistency of the link geometry, while the hydrodynamic lift force varies due to the changing orientation of the algal filament bundle link in space.

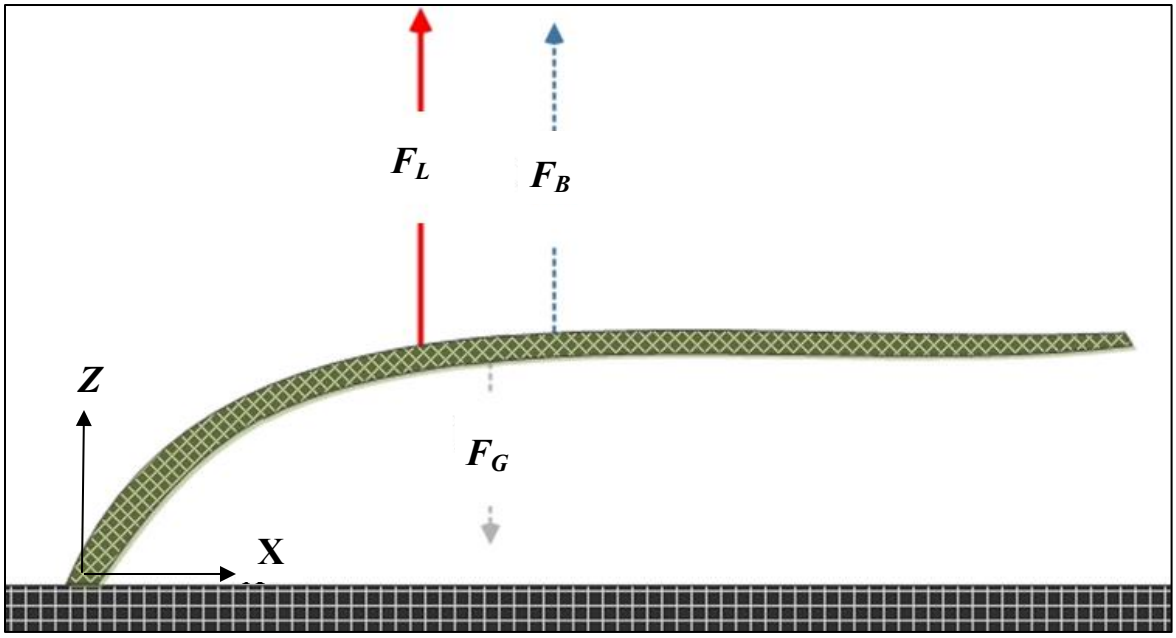

Figure 10: Vertical forces on an algal filament bundle.

The first group of forces includes the force of gravity (equation (6)).

$$F_G = \rho_p \forall_k g \tag{6}$$

where F_G is the force on the filament bundle due to weight [N], ρ_p is the algal filament bundle density [g/m^3], and $\forall_k$ is the volume of the algal filament bundle [m^3], and g is the acceleration due to gravity [m/s^2]. The next constant force in this sub-group includes the force of buoyancy (equation (7)).

$$F_B = \rho \forall_k g \tag{7}$$

where F_B is the force of buoyancy on the algal filament bundle [N] (Hondzo and Wang 2002), ρ is the fluid density [kg/m^3], and $\forall_k$is the volume of the tapered cylinder algal filament bundle link [m^3], and g is the acceleration due to gravity [m/s^2]. The hydrodynamic lift force varies due to the orientation of the algal filament bundle and can be described by equation (8)

$$F_L = \frac{\rho}{2} A_p C_L \mathrm{U}_*^2 \tag{8}$$

where F_L is the hydrodynamic lift force [N] (Hondzo and Wang 2002), ρ is the fluid density [kg/m^3], A_p is the algal filament bundle link planar area [m^2], C_L is the lift coefficient [dimensionless], U_* is the friction velocity [m/s].

The planar area is a function of the projected area of the algal filament bundle onto the horizontal plane (Figure 11). In this study the planar area takes on the form of a trapezoidal area which was calculated in Appendix A.

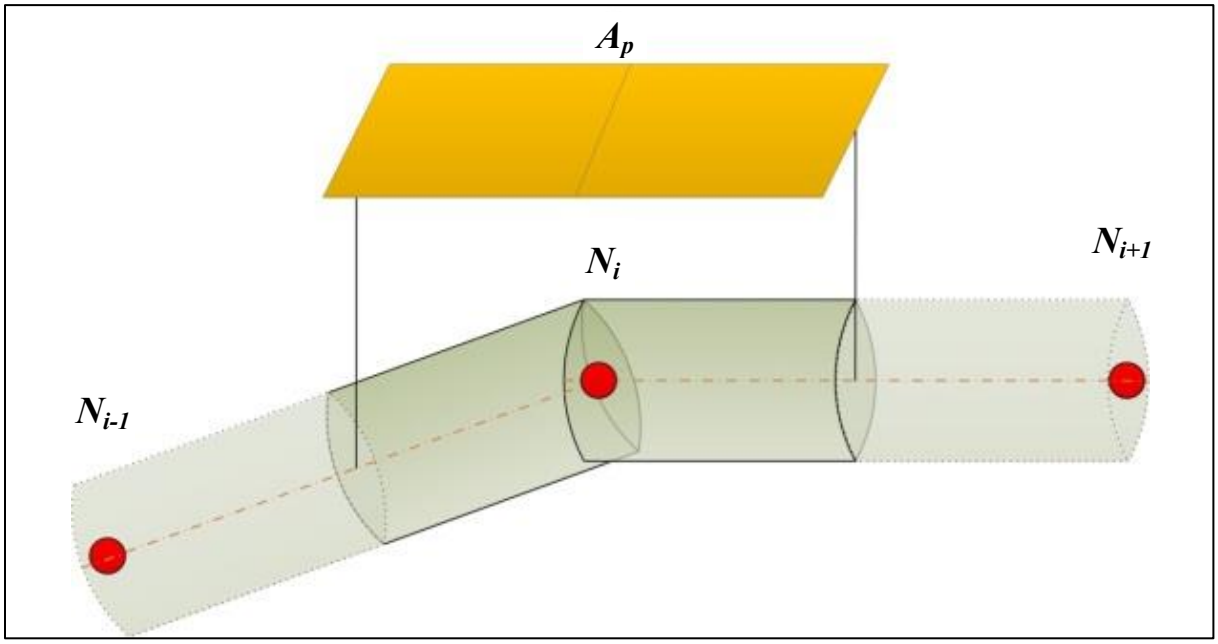

Figure 11: Lift force planar area clarification schematic.

The hydrodynamic lift coefficient is similar in principle to the drag force coefficient. However, instead of being a function of the flow regime, it can be attributed to the orientation of the cylindrical algal filament bundle link (Malavasi and Blois 2012). Hydrodynamic lift is

created by the difference in pressure from the difference in velocity traveling above and below an object in a flow. This phenomenon has been observed in studies of velocity profile changes resulting from the variation of orientation angle or pitch to the oncoming flow (Malavasi and Zappa 2009). The differences in flow conditions above and below the cylinder produce a pressure gradient and a lift is produced. The third parameter is the friction velocity which is a function of the vertically varying velocity due to the logarithmic velocity profile of the oncoming horizontal flow.

2.2.0: Background: Finite Element Modeling

2.2.1: Equations of Free Body Motion

The types of forces previously discussed are those which externally act upon the algal filament bundle. However, the motion of the algal filament bundle itself also provides an additional family of forces which may cause fatigue and failure of the algal filament ultimately resulting in the occurrence of sloughing.

Various finite element regimes that could be used with motion tracked data include a free body mass application, application of a rotational spring at the nodes, or rigid body transformation analysis (Bathe 1982). The method chosen to define finite element mechanics was a frame-type system because it would provide the easiest method to extract values of structure tension from the simulation results (Thai and Kim 2012). A benthic filament bundle can be thought of as an assemblage of ideal mass elements each of which can move when a force is placed on it (Denny and Hale 2003), as seen in Figure 12.

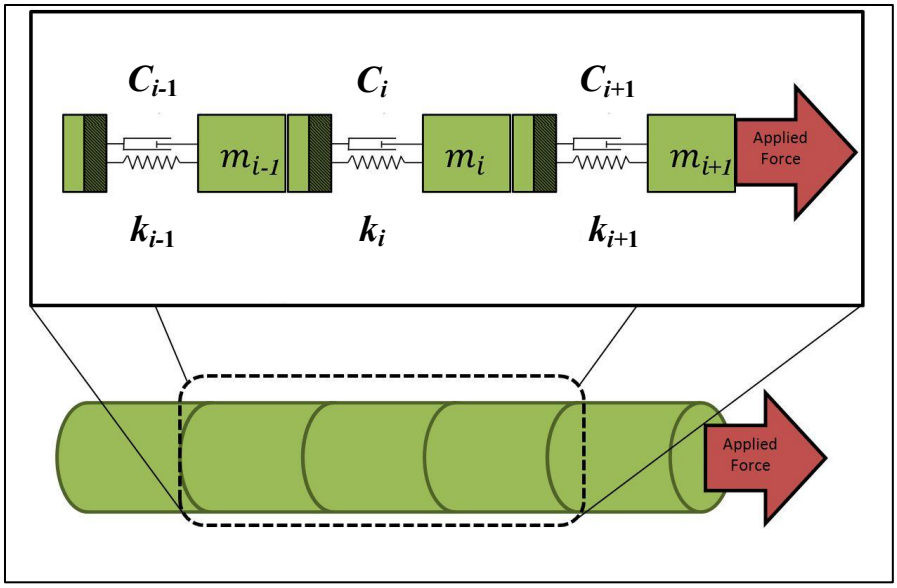

Figure 12: 1-D mass spring dampener system schematic.
The dynamic horizontal system contains a mass *m* coupled with a spring constant *k* and a dampener coefficient *c*.

The mathematical system was chosen with a dampener because the movements of the algal filament bundle do no oscillate continuously once a force is exerted from experimental observation. The combination of the spring and dampener in the system is directly proportional to the tension strength of the algal filament bundle in response to the external forces applied to it. To model the dynamics of the mass spring dampener system, the equations of motion are used to describe the acceleration, velocity and displacement of this system (equation (9)) (Bathe 1982).

$$m_i\ddot{x} + c_i\dot{x} + k_i x = F_x(t) \qquad (9)$$

where m_i is the mass element [kg], $\ddot{x}$ is the horizontal acceleration of the mass element [m/s^2], c_i is the dampening coefficient [kg/s], $\dot{x}$ horizontal velocity of the mass element [m/s], k_i is the spring constant [kg/s^2], x is the horizontal displacement [m], F_x is the applied horizontal force on the mass element [kg m/s^2], and *t* is time. To model the way a benthic filament bundle node

moves in a two dimensional domain would require a similar system seen in equation (9) but in the vertical direction, as seen in equation (10).

$$m_i\ddot{z} + c_i\dot{z} + k_i z = F_z(t) \qquad (10)$$

where m_i is the mass element [kg], $\ddot{z}$ is the vertical acceleration of the mass element [m/s^2], c_i is the dampening coefficient [kg/s], $\dot{z}$ vertical velocity of the mass element [m/s] , z is the vertical displacement [m], F_z is the applied vertical force on the mass element, and t is the time the force calculation was taken. Note that the coefficients of the spring and dampener system are the same as in equation (9) signifying an assumption that the structural properties of the algal filament bundle are isotropic (the same in any given direction). This phenomenon was not confirmed but was merely adopted for mathematical simplicity under this study.

The application of the mass spring dampener system can be applied to a specific point on an algal filament bundle as it moves in a specific direction due to an imposed force. The combination of the spring and dampener system in unison behaves like the internal structural resistance of the benthic filament bundle. The internal forces can be modeled using equation (11).

$$F_C = \sigma_c \frac{\pi\phi^2}{4} \qquad (11)$$

where F_C is the resultant force from F_x and F_z on the algal filament bundle attachment force [N], σ_c is the internal stress on the algal filament [N/m^2], and ϕ is the algal filament bundle diameter at the node [m].

The system increases in complexity with each node added to the system because there would be an additional two degrees of freedom per node. The increase in mathematical

complexity can be seen in Figure 13 which shows that there must be two-spring dampener system attached in each direction to the mass. Therefore, each node can move in two directions, yet the location of a specific mass node is dependent on the position of the previous mass node. Modeling this system would require solving a system of matrices which have the dimension of "n" nodes which would be computationally very heavy under a large number of nodes. However, in this research study a small number of nodes were chosen to allow checking the finite difference simulation by hand to ensure the expected convergence and proof of concept.

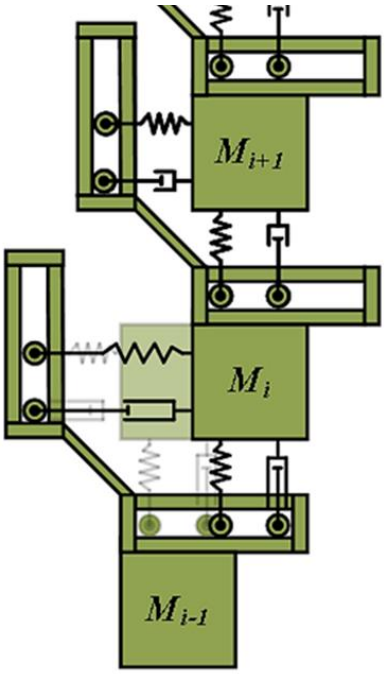

Figure 13: Coupled two degree of freedom per node system illustration schematic.
Looking at an algal filament bundle, it can be modeled as a system of interdependent mass spring dampeners.

To maintain simplicity in the model, it is assumed that the dampener spring system would act as two independent horizontal and vertical systems which can be seen with Figure 14. This can be done because there are types of forces which are assumed to work independently in each direction. In the horizontal direction, there are only the imposed forces of fluid drag and the

reactive axial tension of the filament bundle at play. In the vertical direction, there are the imposed forces which act on the structural property of bending strain on the filament bundle.

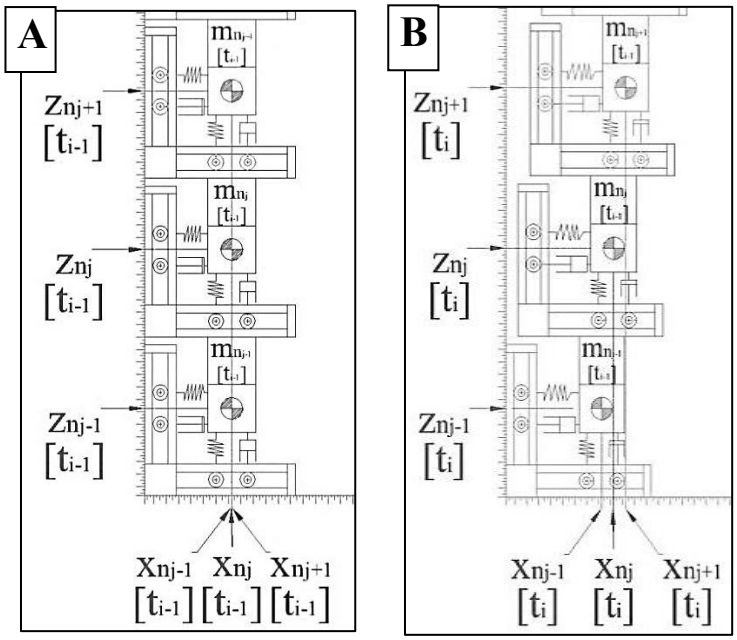

Figure 14: Assumption of direction independence in mass spring dampener system.
(A) : Initial vertical position configuration of mass spring dampener system; (B) A force has been exerted on mass "m_i", resulting in a slight displacement in that specific node and onward in comparison to figure (A). Note: that the horizontal system has been changed dynamically making the horizontal spring dampener system become stretched, while leaving the vertical spring dampener system of the specific node unaffected.

The physics of the benthic filament bundle system can be modeled for a given set of "n" nodes in the horizontal "x" and vertical "z" using two systems seen in Equation (12) and (13).

$$\begin{bmatrix} m_1 & 0 & \cdots & 0 \\ 0 & m_2 & \cdots & 0 \\ \vdots & \vdots & \ddots & \vdots \\ 0 & 0 & \cdots & m_n \end{bmatrix} \begin{bmatrix} \ddot{x}_1 \\ \ddot{x}_2 \\ \vdots \\ \ddot{x}_n \end{bmatrix} + \begin{bmatrix} c & 0 & \cdots & 0 \\ 0 & c & \cdots & 0 \\ \vdots & \vdots & \ddots & \vdots \\ 0 & 0 & \cdots & c \end{bmatrix} \begin{bmatrix} \dot{x}_1 \\ \dot{x}_2 \\ \vdots \\ \dot{x}_n \end{bmatrix} + \begin{bmatrix} k & 0 & \cdots & 0 \\ 0 & k & \cdots & 0 \\ \vdots & \vdots & \ddots & \vdots \\ 0 & 0 & \cdots & k \end{bmatrix} \begin{bmatrix} x_1 \\ x_2 \\ \vdots \\ x_n \end{bmatrix} = \begin{bmatrix} F_{x_1} \\ F_{x_2} \\ \vdots \\ F_{x_n} \end{bmatrix} \qquad (12)$$

$$\begin{bmatrix} m_1 & 0 & \cdots & 0 \\ 0 & m_2 & \cdots & 0 \\ \vdots & \vdots & \ddots & \vdots \\ 0 & 0 & \cdots & m_n \end{bmatrix} \begin{bmatrix} \ddot{z}_1 \\ \ddot{z}_2 \\ \vdots \\ \ddot{z}_n \end{bmatrix} + \begin{bmatrix} c & 0 & \cdots & 0 \\ 0 & c & \cdots & 0 \\ \vdots & \vdots & \ddots & \vdots \\ 0 & 0 & \cdots & c \end{bmatrix} \begin{bmatrix} \dot{z}_1 \\ \dot{z}_2 \\ \vdots \\ \dot{z}_n \end{bmatrix} + \begin{bmatrix} k & 0 & \cdots & 0 \\ 0 & k & \cdots & 0 \\ \vdots & \vdots & \ddots & \vdots \\ 0 & 0 & \cdots & k \end{bmatrix} \begin{bmatrix} z_1 \\ z_2 \\ \vdots \\ z_n \end{bmatrix} = \begin{bmatrix} F_{z_1} \\ F_{z_2} \\ \vdots \\ F_{z_n} \end{bmatrix} \quad (13)$$

As more subsequent repeating of these mass dampener node units are incorporated into the model, the final result approaches a closer physical representation of a flexible filament bundle. The repeated use of frame elements under a small spatial step approaches the behavior of a cable.

2.2.2: Numerical Calculations of Equations of Motion

For the sake of simplicity and clarity, only horizontal deformations will be shown for only three nodes that start at a vertical alignment geometry (Figure 15).

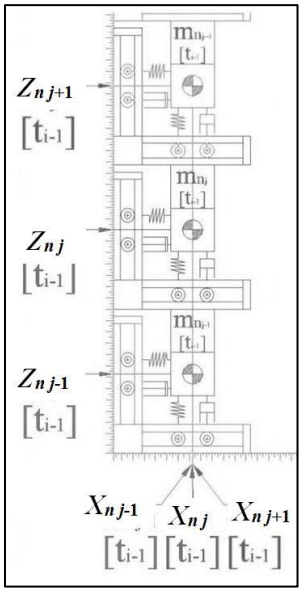

Figure 15: Mass spring dampener system schematic.

The horizontal equation of motion for the initial node of the benthic filament of Figure 15 is represented by the equation of motion given a force at the initial time in Equation (14).

$$F_{x_{j-1}} = x_{j-1}k + \dot{x}_{j-1}c + \ddot{x}_{j-1}m_{j-1} \tag{14}$$

The complete system of equations which represents all three node elements from Figure 15 at the initial time period can be seen in Equation (15).

$$\begin{aligned} F_{x_{n_{j-1,}[t_{i-1}]}} &= x_{n_{j-1,}[t_{i-1}]}\, k_{n_{j-1}} + \dot{x}_{n_{j-1,}[t_{i-1}]}\, c_{n_{j-1}} + \ddot{x}_{n_{j-1,}[t_{i-1}]}\, m_{n_{j-1}} \\ F_{x_{n_{j,}[t_{i-1}]}} &= x_{n_{j,}[t_{i-1}]}\, k_{n_{j-1}} + \dot{x}_{n_{j,}[t_{i-1}]}\, c_{n_{j-1}} + \ddot{x}_{n_{j,}[t_{i-1}]}\, m_{n_j} \qquad etc \\ F_{x_{n_{j+1,}[t_{i-1}]}} &= x_{n_{j+1,}[t_{i-1}]} k_{n_{j-1}} + \dot{x}_{n_{j+1,}[t_{i-1}]} c_{n_{j-1}} + \ddot{x}_{n_{j+1,}[t_{i-1}]} m_{n_{j+1}} \end{aligned} \tag{15}$$

After the initial start of time in the simulation, the applied force on the entire mass node deforms the structure slightly, and each of the mass node units moves slightly before the next time-step.

Looking at only the initial mass node (spatially referenced as "j-1") with each subsequent snapshot through time, a new equation can be made with each subsequent time sequence and the subsequent series can be seen in Equation (16).

$$\begin{aligned} F_{x_{j-1,[t_{i-1}]}} &= x_{j-1,[t_{i-1}]}k + \dot{x}_{j-1,[t_{i-1}]}c + \ddot{x}_{j-1,[t_{i-1}]}m_{j-1} \\ F_{x_{j-1,[t_i]}} &= x_{j-1,[t_i]}k + \dot{x}_{j-1,[t_i]}c + \ddot{x}_{j-1,[t_i]}m_{j-1} \\ F_{x_{j-1,[t_{i+1}]}} &= x_{j-1,[t_{i+1}]}k + \dot{x}_{j-1,[t_{i+1}]}c + \ddot{x}_{j-1,[t_{i+1}]}m_{j-1} \\ F_{x_{j-1,[t_{i+2}]}} &= x_{j-1,[t_{i+2}]}k + \dot{x}_{j-1,[t_{i+2}]}c + \ddot{x}_{j-1,[t_{i+2}]}m_{j-1} \\ &\vdots \\ F_{x_{j-1,[t_n]}} &= x_{j-1,[t_n]}k + \dot{x}_{j-1,[t_n]}c + \ddot{x}_{j-1,[t_n]}m_{j-1} \end{aligned} \tag{16}$$

The velocity results from Equation (16) can be calculated with the following series seen in Equation (17).

$$
\begin{aligned}
\dot{x}_{j-1,[t_i]} &= \frac{x_{j-1,[t_i]} - x_{j-1,[t_i]}}{(t_i - t_{i-1})} \\
\dot{x}_{j-1,[t_{i+1}]} &= \frac{x_{j-1,[t_{i+1}]} - x_{j-1,[t_{i+1}]}}{(t_{i+1} - t_i)} \\
\dot{x}_{j-1,[t_{i+2}]} &= \frac{x_{j-1,[t_{i+2}]} - x_{j-1,[t_{i+2}]}}{(t_{i+2} - t_{i+1})} \\
&\vdots \\
\dot{x}_{j-1,[t_n]} &= \frac{x_{j-1,[t_n]} - x_{j-1,[t_n]}}{(t_n - t_{n-1})}
\end{aligned}
\tag{17}
$$

Note that the initial velocity cannot be calculated due to lack of temporal data which doesn't exist before the initial time. The acceleration results from Equation (16) can be calculated with the following series seen in Equation (18).

$$
\begin{aligned}
\ddot{x}_{j-1,[t_i]} &= \left(\frac{\left(x_{j-1,[t_{i+1}]} - x_{j-1,[t_i]}\right)}{(t_{i+1} - t_i)} - \frac{\left(x_{j-1,[t_i]} - x_{j-1,[t_{i-1}]}\right)}{(t_i - t_{i-1})} \right) / (t_{i+1} - t_{i-1}) \\
\ddot{x}_{n_{j-1,[t_{i+1}]}} &= \left(\frac{\left(x_{j-1,[t_{i+2}]} - x_{j-1,[t_{i+1}]}\right)}{(t_{i+2} - t_{i+1})} - \frac{\left(x_{j-1,[t_{i+1}]} - x_{j-1,[t_i]}\right)}{(t_{i+1} - t_i)} \right) / (t_{i+2} - t_i) \\
\ddot{x}_{n_{j-1,[t_{i+2}]}} &= \left(\frac{\left(x_{j-1,[t_{i+3}]} - x_{j-1,[t_{i+2}]}\right)}{(t_{i+3} - t_{i+2})} - \frac{\left(x_{j-1,[t_{i+2}]} - x_{j-1,[t_{i+1}]}\right)}{(t_{i+2} - t_{i+1})} \right) / (t_{i+3} - t_{i+1}) \\
&\vdots \\
\ddot{x}_{n_{j-1,[t_{n-1}]}} &= \left(\frac{\left(x_{j-1,[t_{n-1}]} - x_{j-1,[t_{n-2}]}\right)}{(t_{n-1} - t_{n-2})} - \frac{\left(x_{j-1,[t_{n-2}]} - x_{j-1,[t_{n-3}]}\right)}{(t_{n-2} - t_{n-3})} \right) / (t_{n-1} - t_{n-3})
\end{aligned}
\tag{18}
$$

Note that the initial and final acceleration cannot be calculated due to lack of spatially time referenced data at the beginning and end node points.

A minimum of four time referenced data points must be needed for a single calculated value of the mass dampener and spring coefficient for each mass dampener spring coefficient node. The algorithm for solving the spring and dampener coefficients and obtain value of internal forces can be seen in Appendix A: section 6. The internal forces for a benthic filament of n nodes results in Equation (23) (Chopra 2001).

$$\begin{bmatrix} F_{\sigma_{j-1},[t_i]} \\ F_{\sigma_j,[t_i]} \\ \vdots \\ F_{\sigma_N,[t_i]} \end{bmatrix} = k \begin{bmatrix} 2 & -1 & 0 & \dots \\ -1 & 2 & -1 & 0 \\ 0 & -1 & \ddots & 0 \\ \vdots & 0 & -1 & 2 \end{bmatrix} \begin{bmatrix} x_{j-1,[t_i]} - x_{j-1,[t_{i-1}]} \\ x_{j,[t_i]} - x_{j,[t_{i-1}]} \\ \vdots \\ x_{N,[t_i]} - x_{N-1,[t_{i-1}]} \end{bmatrix} \tag{19}$$

Solving for the internal stress is done by dividing the internal force by the specified cross sectional area as seen in Equation (24) (Chopra 2001).

$$\sigma_{j-1,[t_i]} = \frac{F_{\sigma_{j-1},[t_i]}}{A_{C\,j-1,[t_i]}} \tag{20}$$

The cross sectional area for a node can be calculated using Equation (21), which was derived in Appendix A: section 1.

$$A_{C\,j-1,[t_i]} = \frac{{\phi_{j-1,[t_i]}}^2 \pi}{4\sin(\theta)} \tag{21}$$

Embedding Equation (21) into Equation (24), results in an equation to represent the internal stress of the benthic filament bundle.

$$\sigma_{j-1,[t_i]} = \frac{F_{\sigma_{n_{j-1}},[t_i]} 4\sin(\theta)}{{\phi_{j-1}}^2 \pi} \tag{22}$$

2.3.0: Background: Motion Tracking

The purpose of motion tracking is to bridge the application of mathematical modeling and physical experimentation. The ability to quantify and track an object using a camera is an essential tool to bridge these two distinct models successfully.

2.3.1: Object Based Motion Tracking

To investigate the benthic filament bundle structure in depth, visually captured data could be taken (Ishino and Ishikawa 2001) and converted into spatially referenced and recorded data to

be analyzed (Bhat, Seitz et al. 2002). Typical data that can be recorded from video capture footage of algal filament bundles in a fluid flow environment are included in Table 3.

Table 2: List of spatial data extracted from motion tracked footage.

Parameter Measured	Parameter Description
Nodes	Spatially and temporally reference node markers on filament
Fluid dye velocity	Fluid dye velocity tests to derive velocity profile
Filament diameter	Filament diameter at a given node along length of filament
Filament link length	Paired nodes provide a filament distance

In video capture, an image, no matter what the size, is usually broken up into segments to be analyzed in discrete packets (Hui, Wen et al. 2012). The typical size of these finite segments is approximately 8 × 8 pixels. A typical video frame consists of a variety of colors, and a number is associated with each pixel that correspond to the color and intensity (Kikuchi, Abe et al. 2012). Similar colors share similar pixel numerical values. Therefore a collection of numerical pixels against a contrasted background can be identified easily as an object through programming (Khan, Gu et al. 2011). When a program identifies an object, it can then track that object as it moves through space by tracking the image frames that have passed by through a calibrated pixelated distance.

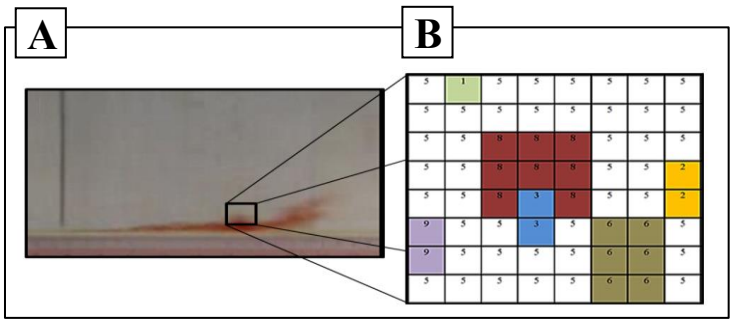

Figure 16: Numerical pixel image concept schematic.

The most ideal situation in motion tracking an object in a two dimensional plane is if that object did not alter its shape and is consistently a color that contrasts its background. An example of this situation can be seen in

Figure 17, which show two time-referenced images of a red object from a video represented by a red rectangle against a white background which has moved two pixels to the right between video frames.

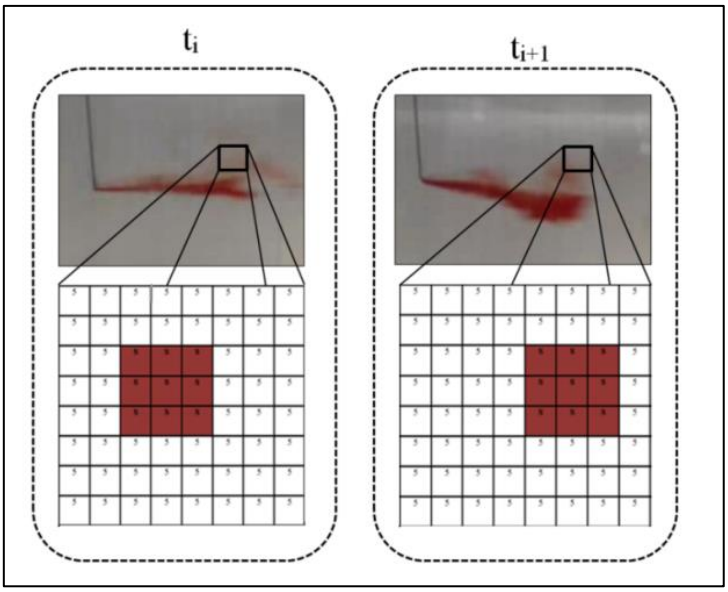

Figure 17: Motion capture of pixilated object through time referenced image frames.

The overall procedure of motion capture involves filming the filament in motion and then implementing the use of motion tracking algorithms on a particular point of interest within the footage. The objects tracked through a pixelated distance should then be calibrated to a known distance within the field of view and the results saved for future use.

3.0: Materials and Methods

3.1.1: Logarithmic Velocity Profile Formulation

The first application of motion tracking was to develop the logarithmic velocity profile of the fluid flow. The flow in the apparatus set-up was assumed to be uniform in the horizontal direction and vary in a logarithmic fashion in the vertical direction. The apparatus used was a foot long as seen in Figure 18.

Figure 18: Recirculating flume apparatus used for creating ideal horizontal flow conditions.

To have a rough estimation of the velocity profile, a series of dye tests were made by injecting a contrasting colored dye against a plain background and motion track the head of each plume to calculate a value at specific intervals along the vertical axis. The red #40 propylene

glycol food color dye (McCormick and Company, Sparks, Maryland) was used. A picture of the experimental application of the food color dye can be seen in Figure 19.

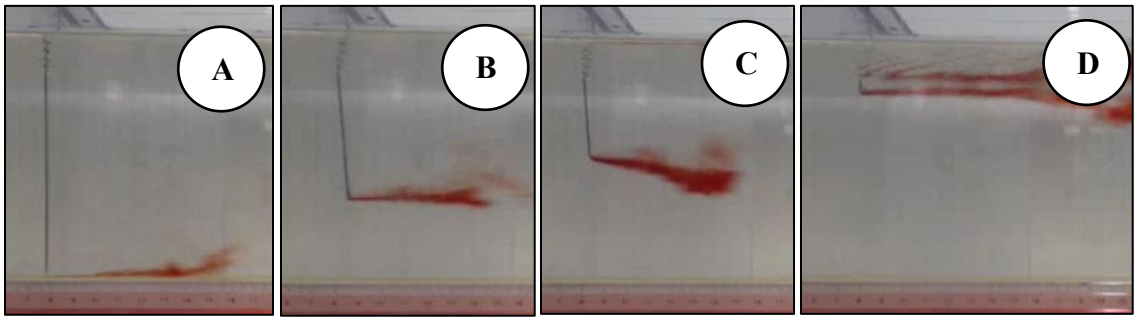

Figure 19: Fluid velocity dye tests in circulating flume at different heights.

The dye is isobuoyant thus, the movement of the dye would be representative of the fluid flow velocity. A thin application needle (2 mm diameter) was used to limit the effect of fluid flow velocity on the speed of the applied dye. The motion tracking program recorded the height of the start of where the tip of the injection needle would be and later record the horizontal speed of the injected dye plume. The recording of multiple set of velocities across the vertical axis were to fit a logarithmic profile to ensure a continuous set of values across the entire depth of the water column. The width of the channel was 0.15 meter and the critical flow rate was measured to be 1.26×10^{-3} m^3/s.

The filamentous algae for run one were grown under the same flow rate in a 9 foot recirculating cultivation flume (

Figure 20 and

Figure 21). The filamentous algae (*Cladophora glomerata*) were seeded from filamentous algal covered rocks taken from Ellicott Creek in Buffalo Amherst, NY. The growth conditions included a light exposure using two 400 watt light fixture systems (Synergy Lighting,

Bradenton, Florida) utilizing an average intensity of 5,000 lumens per square foot. Each light fixture is capable of producing 4,613 lumens per square foot through the use of eight T5 bloom fluorescent bulbs in each fixture. Each light fixture spreads the light over a plan area of 47 in. × 25.5 inches or 8.3 square feet. Reflectors were implemented to ensure all of the light will reflected onto the algal turf surface, with 1 ft. of travel distance between the light bulbs and the algal turf bed. The nutrient loading was achieved through the use of adding continuous batches of Miracle Grow nutrient solution (Scotts Company, Maryville, Ohio) to have a nitrogen loading rate of 1 gram of nitrogen per square meter per day.

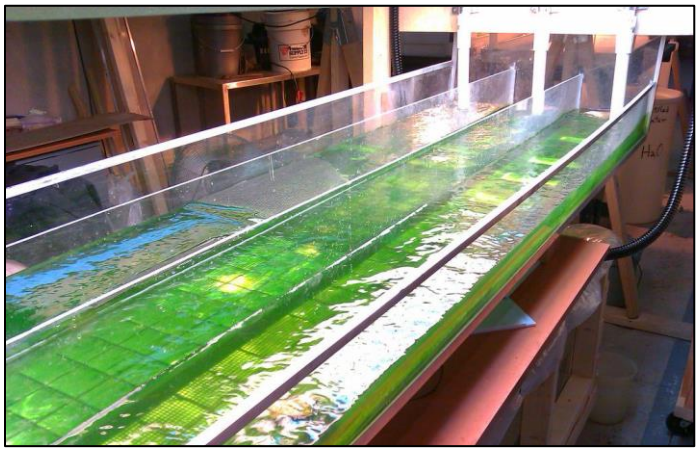

Figure 20: Algal flume used to cultivate filamentous algae for experimental analysis.

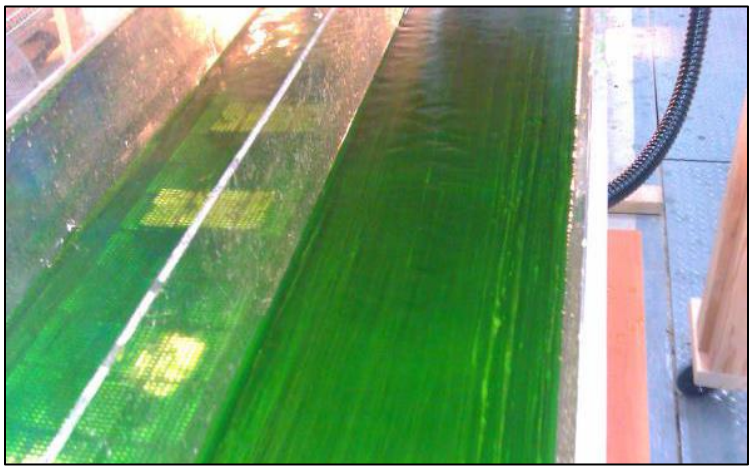

Figure 21: Close up on filamentous algae cultivated in experimental flume apparatus.

A rock was placed in the algal cultivation flume and allowed to be colonized by attached filamentous algae. The rock was then transferred into the horizontal flow flume for motion capture application. To apply the technique of motion capture to the algal filament bundle node motion tracking, the algal filament bundle was stained at specific, measured intervals with a colored dye that would contrast against the green algal filament bundle and environment background. In one such experiment, where there was a desire to divide up the algal filament bundle into four sections, there would be a need to motion track 4 nodes in space simultaneously as seen in Figure 22.

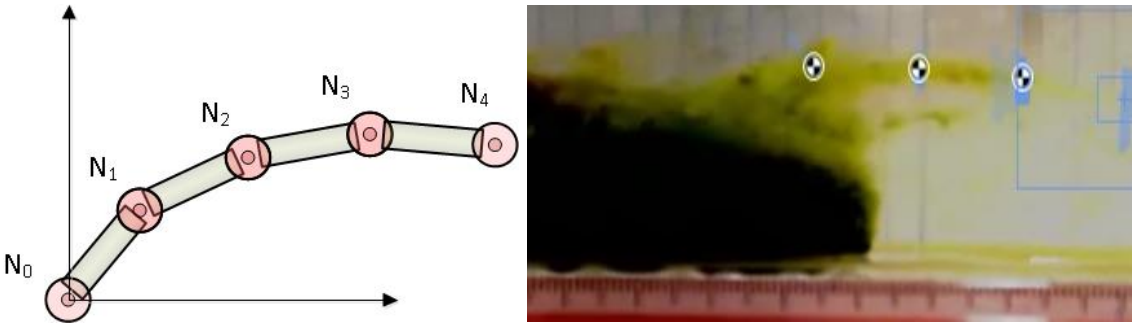

Figure 22: Algal filament bundle node tracking concept schematic.

It was assumed that the base node N_0 does not move throughout the experiment and could therefore serve as the spatial origin. All of the other algal nodes were tracked according to change in pixels to the base node origin. The pixel distances were then calibrated to metric measurements through manual calibrations. The calibrations were done by measuring the pixel distance of an object with a known distance in the video (such as a ruler) and then applying the ratio of video pixel distance to real-world distance to convert all other subsequent measurements.

The motion capture was done using a Logitech HD Pro Webcam C920 utilizing a high definition setting of 1080p at 30 frames-per-second (fps) on an HP Pavilion laptop running a Windows 7 operating system. The video was edited using Windows live video editing software. The motion capture software used was Kinovea version 0.8 which used the video footage in Audio Video Interleave (AVI) format and saved the designated object motion tracking as a Microsoft-Excel XML file. From the dye tests, each of the plumes was motion tracked and a single average velocity was assumed per vertical height at the location where the dye needle first released the dye.

3.1.2: Algal Filament Bundle Link Density

The wet filament bundle volume is measured from the video footage using the calibrated length seen on the screen. The calibrated length was calculated using a ruler placed perpendicular to the line of sight of the camera and then calibrating the ruler length as a basis of distance for all subsequent data recording. The density of the algal filament bundle link cylinder may be considered to be a mixture of both water and algal filament bundle biomass per unit volume. To approximate the density, a weighted average calculation was used. An assumption was then made that the only two things which occupied the algal filament bundle link space were algae biomass and water.

After the flume tests, the algal filament bundle was segmented carefully at the visual nodes markers, rolled into thin cylinders, and left to dry. The dried algal filament bundles were then weighed using a precision scale Model AG245 manufactured by Mettler Toledo accurate to 0.1 mg. The dried volume was then determined by measuring the dry filament bundle diameter and length. The dried algal filament bundle cross-sectional area was calculated by assuming a

constant filament diameter size as seen in Equation (23), which is formally derived in Appendix A: section 5.

$$A_{bc} = \left(\frac{\pi\phi_*^2}{4}\right) * \left[1 + \sum_{i=0}^{q} 6i\right] \quad such\ that: q = \left(\frac{\phi_P}{\phi_*} - 1\right)\frac{1}{2} \tag{23}$$

where ϕ_P is the measured dried bundle filament diameter [m], q is an integer number of concentric ring layers, where a single algal filament is layer zero, ϕ_* is the diameter of a single algal filament [m], and A_{bc} is the overall cross sectional area of each of the algal filaments in the bundle [m].

The difference between the dried filament bundle volume and wet algal filament bundle volume was assumed to be water. The final algal filament bundle density was calculated using Equation (24) where the two densities were weighted according to how much volume each material took up in the given visual volume from the experimental footage.

$$\rho_p = \frac{\rho_B \forall_B + \rho \forall_C}{\forall_p} \tag{24}$$

where ρ_p is the density of the wet periphyton filament bundle [kg/m^3], ρ_B is the density of the dried benthic filament bundle [kg/m^3], $\forall_B$ is the volume of the dried filament bundle [m^3], $\forall_C$ is the volume of water in the wet algal filament bundle [m^3] which is equal to $\forall_p - \forall_B$, and $\forall_p$ is the volume of the overall wet benthic filament bundle.

4.0: Results

4.1.1: Logarithmic Velocity Results

The flow rate of the pump in the measurement flume was set to $1.26\ m^3/s$ with an effective specific discharge of 0.0815 m/s and friction velocity of 0.00815 m/s. The logarithmic velocity profile was calculated using Equation (1) with a roughness length value of 1×10^{-4}m and friction velocity of 8.15×10^{-3} m/s. The dye velocity measurement results and logarithmic model can be seen in Figure 23. The root square mean deviation (RSMD) between the dye velocity measurements and logarithmic velocity model measurements at the same specified intervals was calculated to be 0.023.

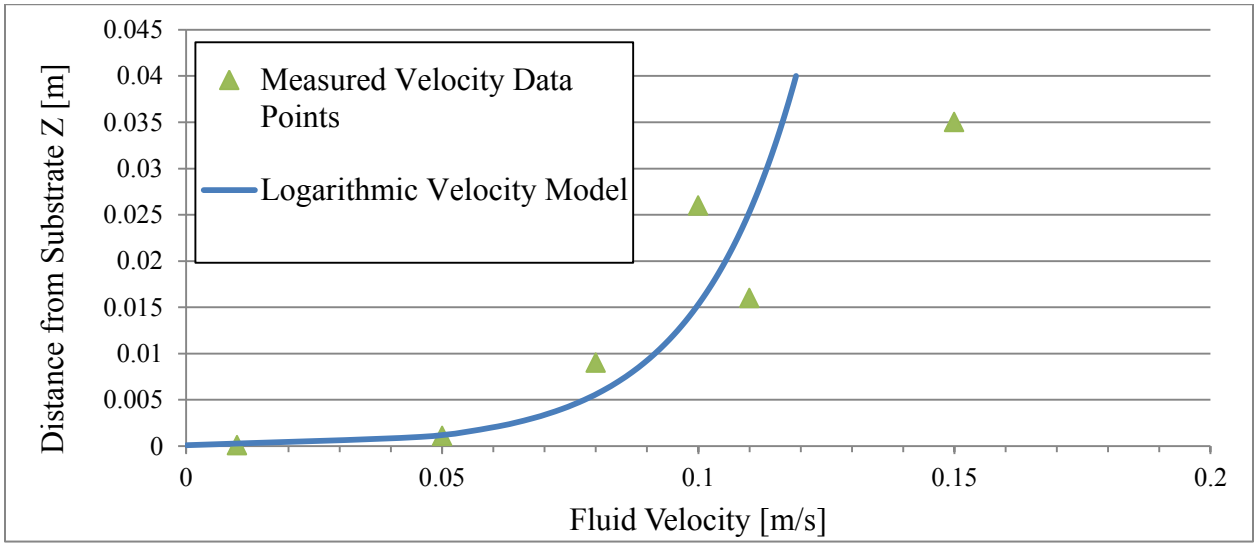

Figure 23: Vertical velocity measurements and model results

The RSMD was 0.8906 between the fitted model and the associated measured data points which can be seen in Figure 24.

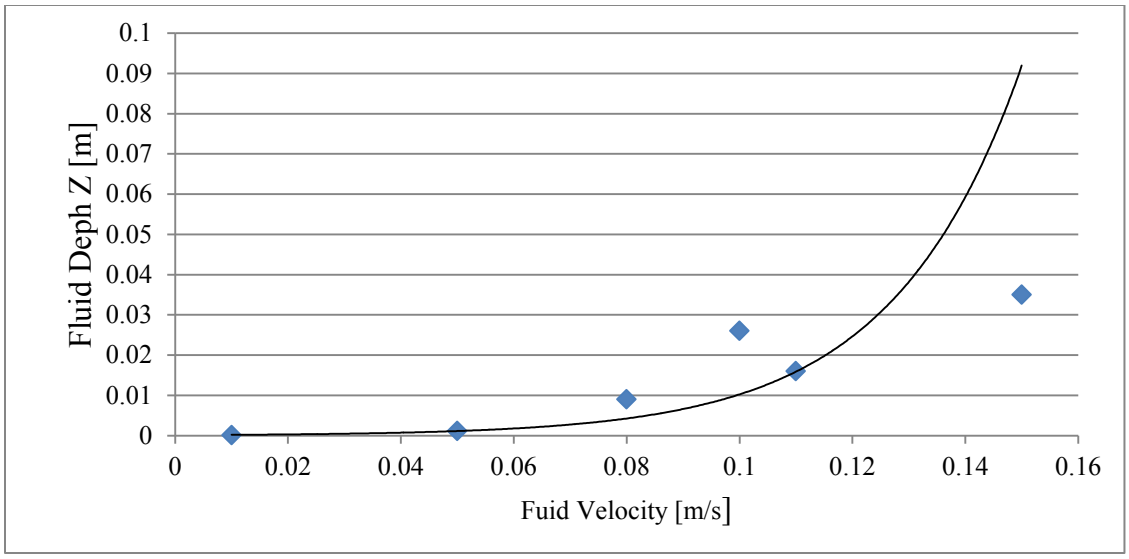

Figure 24: Dye velocity measurement data with fitted logarithmic model.

Comparing the velocity profile model to the fitted logarithmic model can be seen in Figure 25 and resulted in an RSMD of 0.006 between the two logarithmic models.

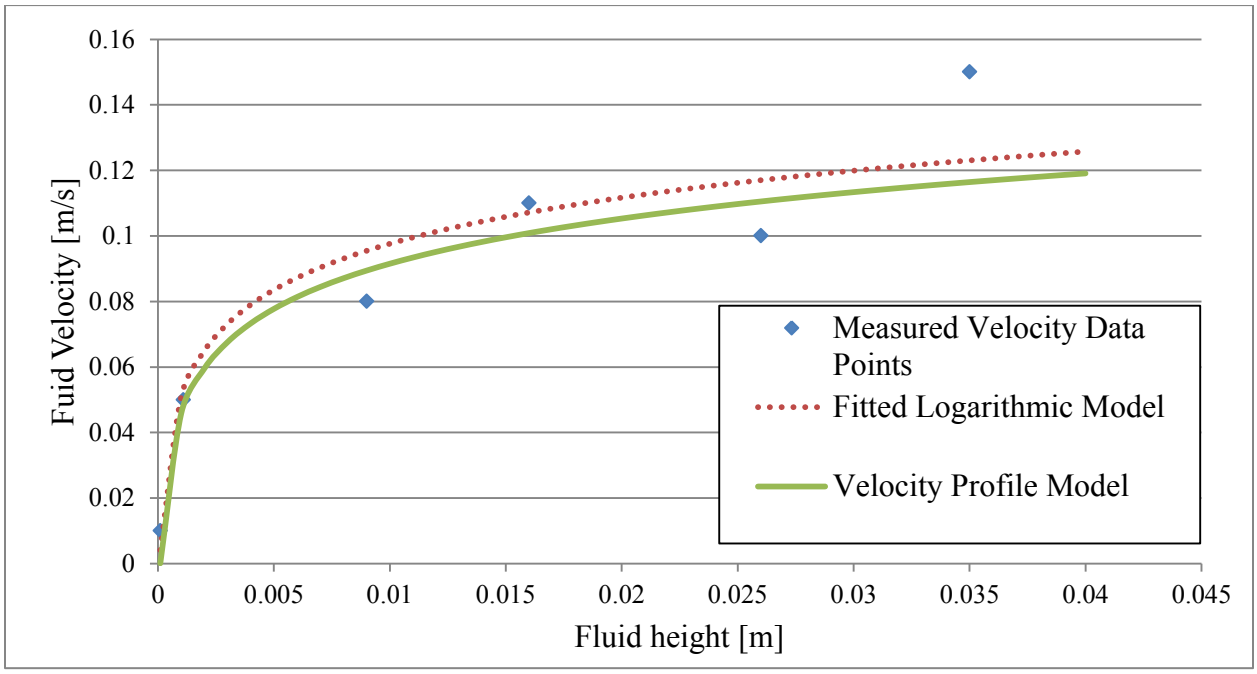

Figure 25: Measured velocity data with fitted model and velocity profile model.

The logarithmic velocity model was used to calculate the Reynolds number vertically across the flume depth and the results can be seen in Figure 26. The characteristic length was found by using the rectangular wetted perimeter of the Plexiglas channel section, and the kinematic viscosity was assumed to be that of water at room temperature.

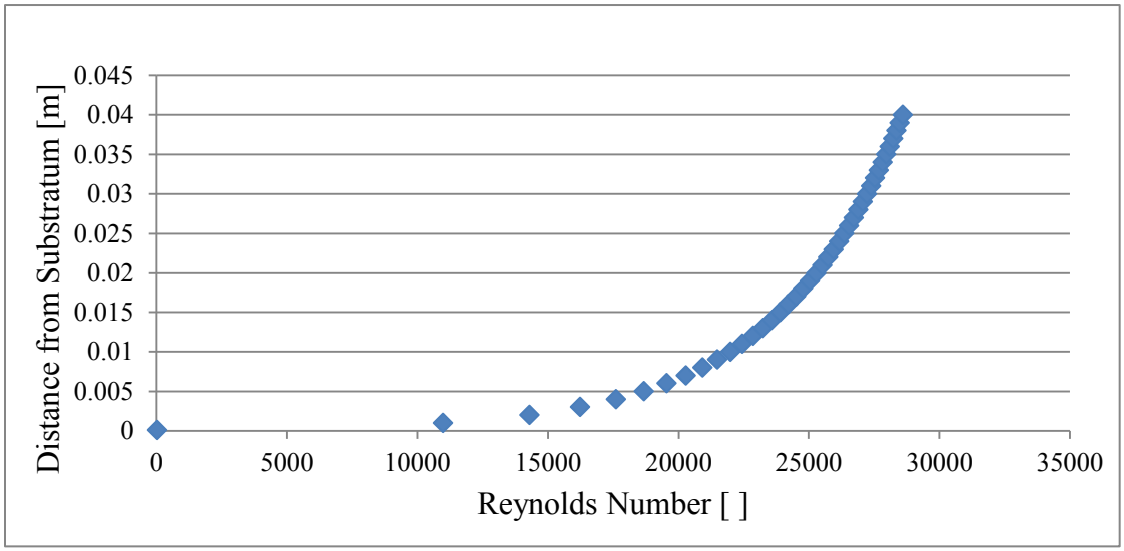

Figure 26: Reynolds number vs. vertical distance.

4.1.2: Object Motion Tracking Results

The motion tracking data consisted of 30 seconds of video footage with a sampling frequency of approximately 30 samples per second. The motion capture sample data set corresponding benthic filament bundle locations on a plane can be seen in Figure 27.

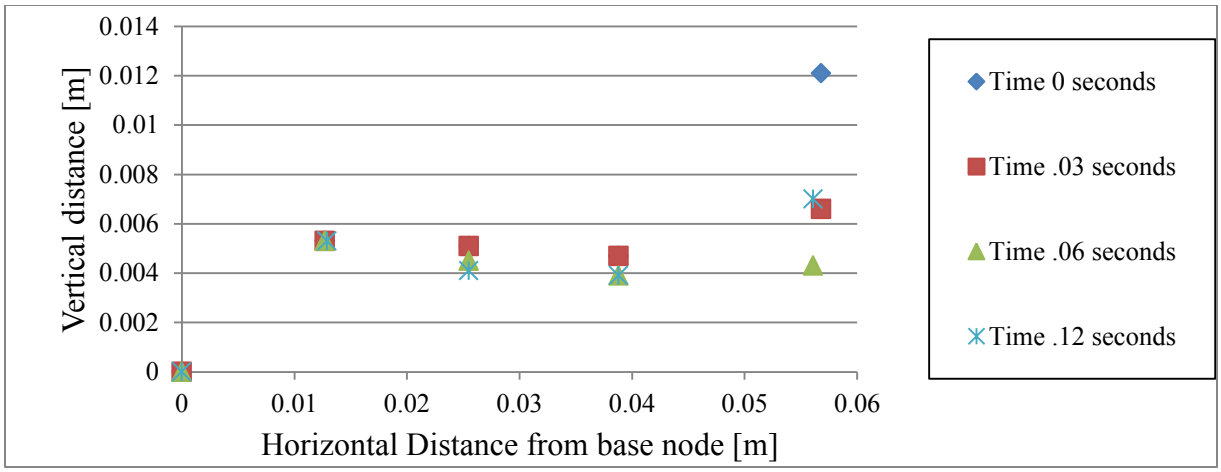

Figure 27: Motion tracked benthic filament bundle nodes through segments in time with initial base node (N_0) as the Cartesian origin.

The complete plotted coordinates of each node for every measurement taken during the full 25 seconds of the experimental video footage can be seen in Figure 28. This figure shows that the relative motion of any filament node is related to the distance of that node from the base node.

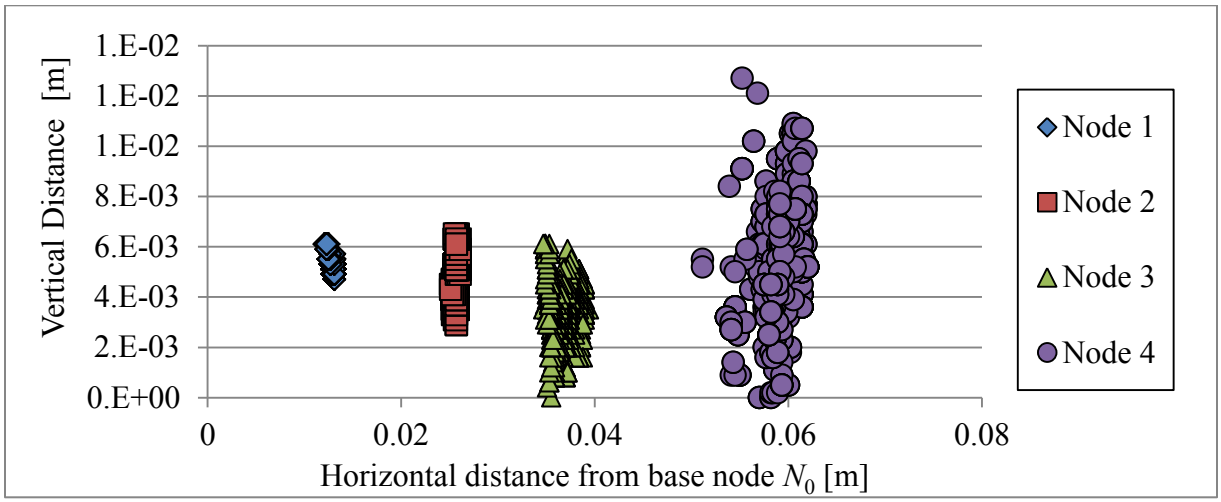

Figure 28: Motion tracked node with initial base node (N_0) as origin.

4.1.3: Fluid-Structure Interaction Model Results

Once the motion tracked data (node number reference, horizontal and vertical position versus time), has been entered into the fluid structural interaction model, the resulting external horizontal and vertical forces on each node can be calculated and plotted, as shown in Figure 29 and Figure 41. The horizontal force was generally greatest and least variable for node 1, and most variable for node 3. The vertical force had a low variance for all nodes, with node 1 exhibiting the greatest and node 3 exhibiting the least.

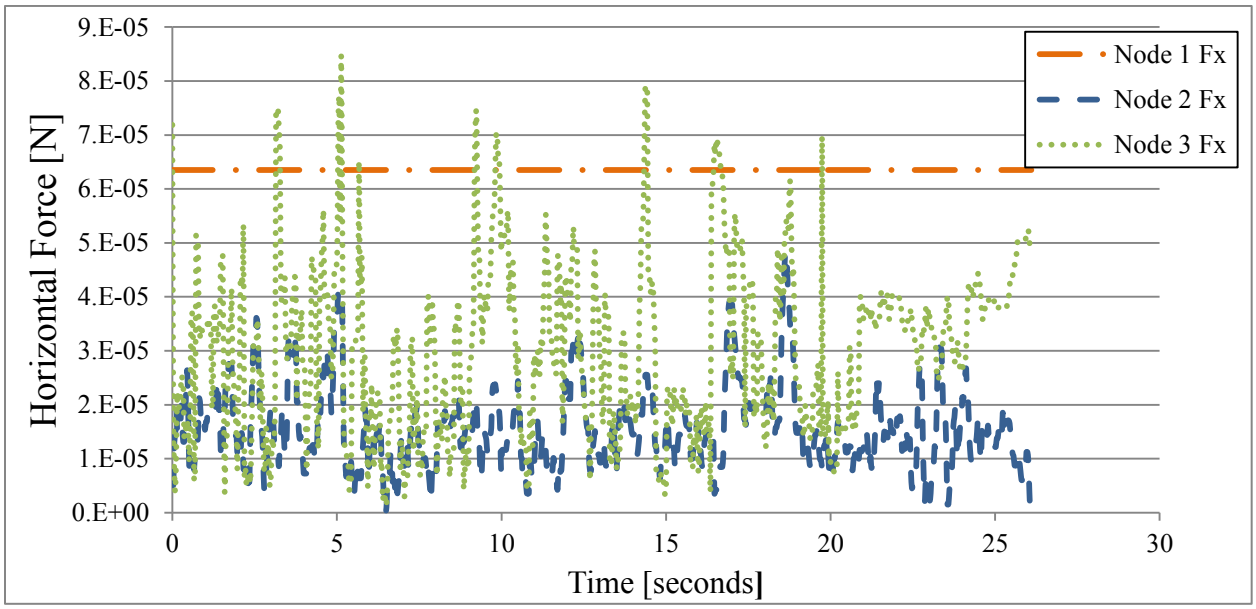

Figure 29: Calculated horizontal force on algal filament bundle nodes versus time.

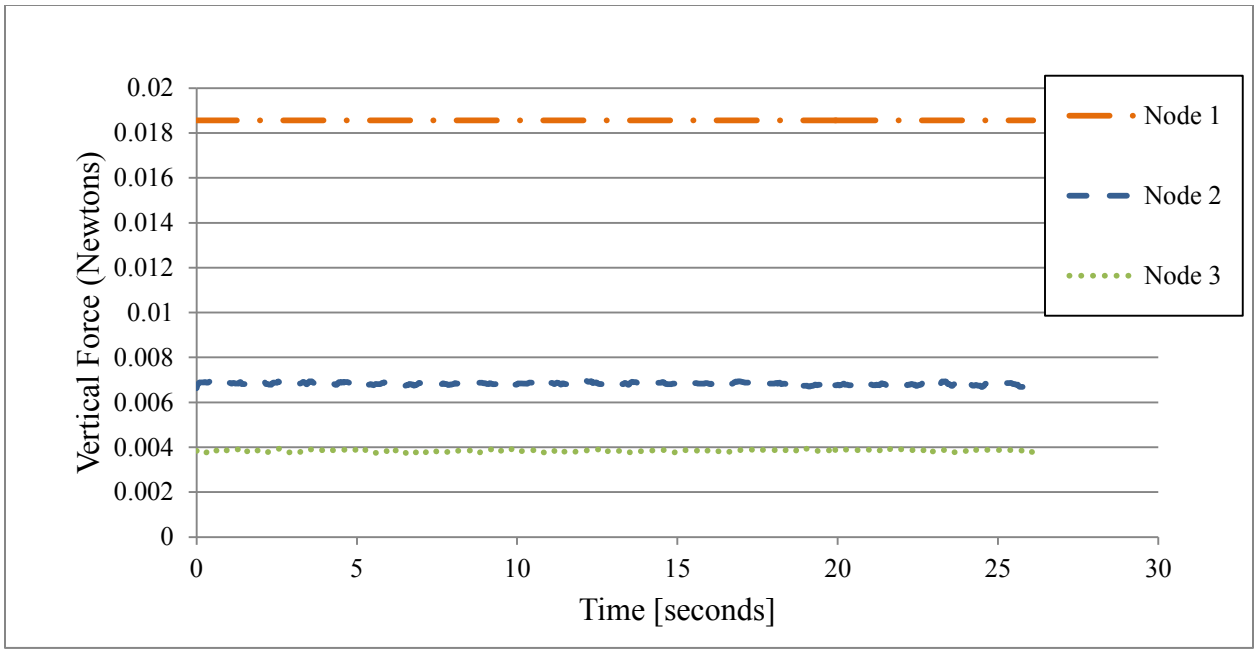

Figure 30: Calculated vertical force on algal filament bundle nodes versus time.

4.1.4: Finite Element Numerical Structure Model Results

Values of the dampener and spring coefficients used in equation (12) and (13) were arbitrarily chosen during the start of each run of the finite-element model. The run continued until the simulated behavior of the nodes behaved similar to the experimental observations. A snapshot of the simulated run of the finite element model can be seen in Figure 31.

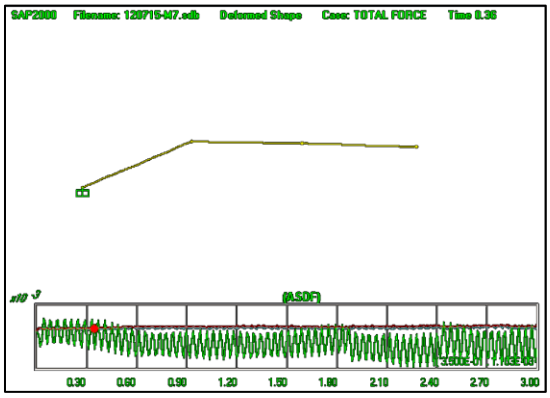

Figure 31: Snapshot from simulation run of the finite element model program SAP2000.

The maximum amount of tensile force the benthic filament exhibited during the finite element model simulations was calculated by dividing the axial force by the cross sectional area of the dried benthic filament bundle at the specified node and reducing the area further by assuming each filament had a benthic filament cell diameter of 75 µm (Johnson, Shivkumar et al. 1996) and eliminating the pore space areas seen in Appendix A section 5. The averaged weighted by node diameter and later averaged between all the nodes was 7.6 MPa. The simulated axial forces from nodes one, two, and three can be seen in Figure 32.

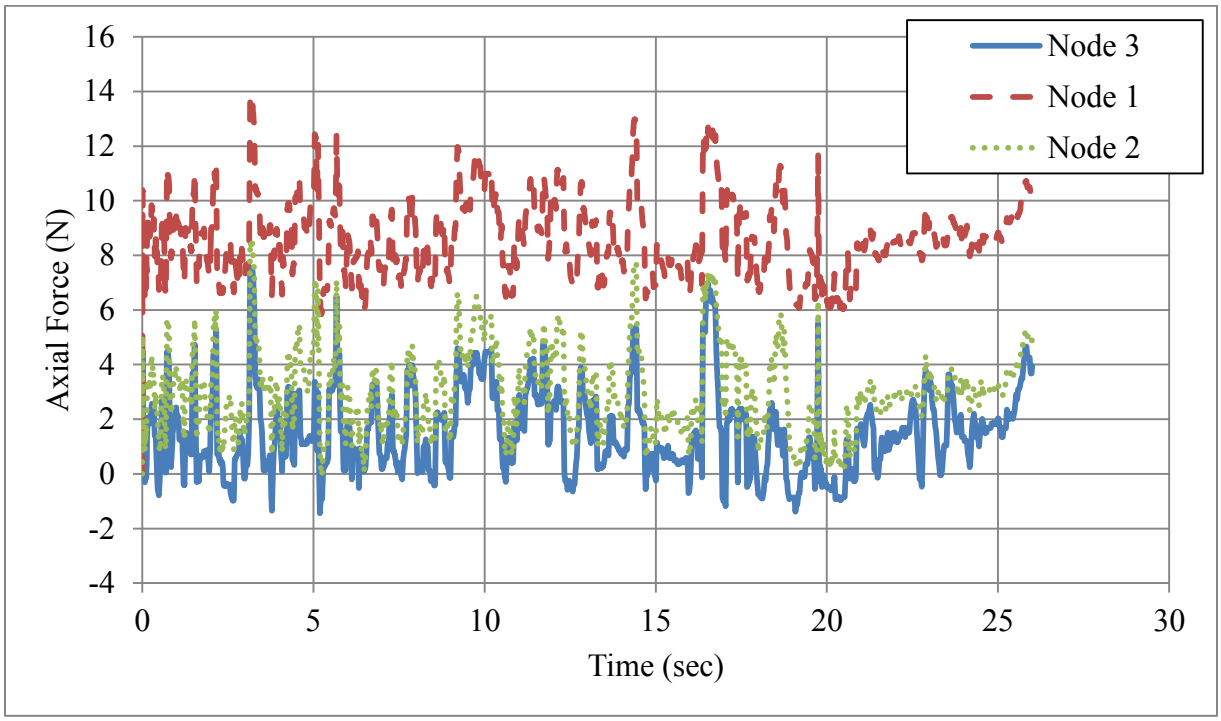

Figure 32: Axial forces on finite element for run 1.

The way in which the runs were evaluated was based on minimizing the difference between the simulated and observed displacements of the benthic filament through a qualitative fashion. The spring and dampener coefficients were varied until the variance of the simulated relative horizontal displacement results were the same as the observed variance of the observed

measurements. Both simulated and experimentally data logged displacements in the horizontal and vertical direction can be seen in

Figure 33 and Figure 34 respectively for node 1.

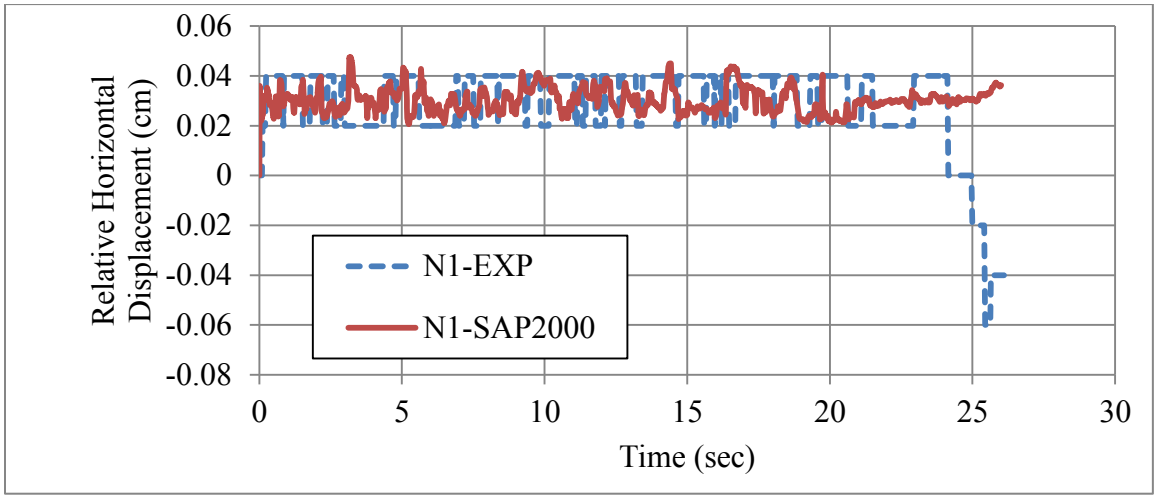

Figure 33: Simulated and data-logged horizontal displacement for node 1.

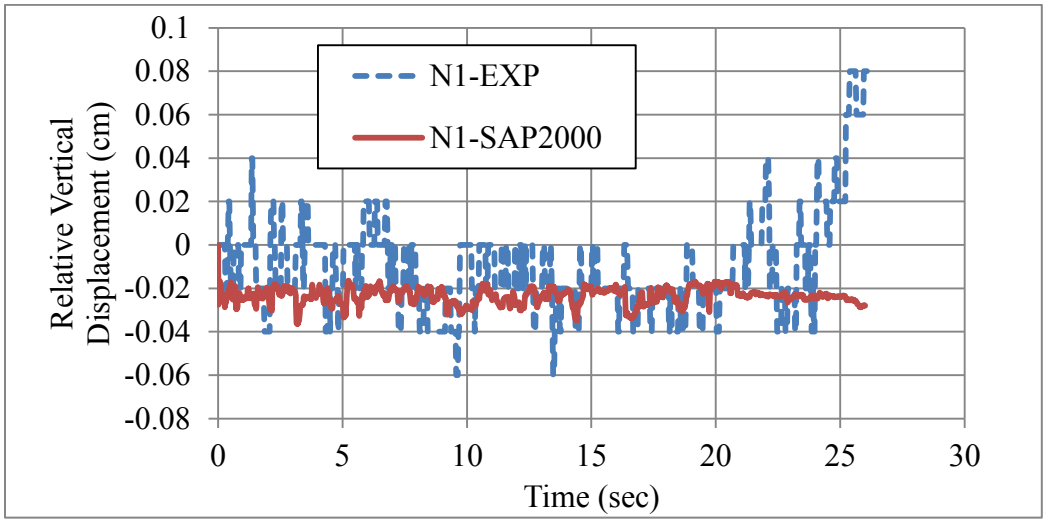

Figure 34: Simulated and data-logged vertical displacement for node 1in run 1.

The process previously discussed of estimating tensile strength values from filamentous algal bundle samples using numerical methods were implemented in triplicate trials from four additional samples. The following results from the experiment procedure can be seen in Table 3.

Table 3: Repeated Data Run Sets

Sample	**1**	Samples taken from controlled experiment fed from constant artificial nutrient solution (Miracle grow) under constant light exposure in wave environment			
Description					
Run	1	644,800	N/m^2	0.6448	Mpa
Run	2	18,700,000	N/m^2	18.7	Mpa
Run	3	3,050,000	N/m^2	3.05	Mpa
Sample	**2**	Samples were taken from a pilot scale plant from downtown buffalo where the effluent water came from Lake Erie and were grown outside in the natural environment			
Description					
Run	1	761767	N/m^2	0.761767	Mpa
Run	2	8721	N/m^2	0.008721	Mpa
Run	3	19836	N/m^3	0.019836	Mpa
Sample	**3**	Samples taken from controlled experiment fed from constant artificial nutrient solution (Miracle grow) under constant light exposure in wave environment			
Description					
Run	1	7,826,800	N/m^2	7.8268	Mpa
Run	2	6,523,788	N/m^2	6.523788	Mpa
Run	3	235,000	N/m^3	0.235	Mpa
Sample	**4**	Samples taken from controlled experiment fed from constant artificial nutrient solution (Miracle grow) under constant light exposure in wave environment			
Description					
Run	1	2,563,400	N/m^2	2.5634	Mpa
Run	2	568,472	N/m^2	0.568472	Mpa
Run	3	6,528,700	N/m^3	6.5287	Mpa

5.0: Discussion

5.1.1: Sources of Error

Before assessing the validity of the final results, an overview of the key assumptions made at critical junctions should first be analyzed. Within the force-interaction model, there was an assumption that the benthic filament bundle links were treated as tapered cylinders because a low number of nodes were chosen. The filament bundle links were treated as tapered cylinders, yet the drag and lift coefficient empirical formulas were based on experimental data collected from the use of straight cylinders. Therefore, the drag and lift coefficients in the fluid interaction model introduce some error in the results because the values correspond to straight cylinder experimental research.

The measurement of the fluid velocity was performed using motion capture and dye tests, but there is some error associated with each procedure. The error associated with the measurement of the fluid velocity profile stems from the presence of the fluid dye needle affecting the incoming flow. There might also be some programming error and noise in the machine vision implementation on tracking objects and creating average velocity values at each height. Another experimental method that perhaps could have reduced the machine vision data logging noise was to use milk as the fluid dye against a black background. This monochromatic technique would have reduced the error in motion tracking by making it very easy to numerically identify a moving object.

The logarithmic velocity profile applied to the model was made in the absence of the algal filament bundle and support structure and therefore may not be the actual velocity profile of the fluid once the specimen and support structure is in place. The filament bundle links, which

are closest to the incoming flow, might experience current velocities similar to the initial measurements. However, the current slows down and is dispersed once it encounters the algal filament and therefore the subsequent links might not have the correct assumed velocity behavior.

A closer look at Figure 28 (which can be seen in Figure 35) reveals that the spatially tracked data seems to fall into distinct rows. The reason for the data separation in the numerical motion capture is due to the fact that the motion capture is based on the movement of pixels and does not track the object continuously through space. Therefore, the bands of data have a discrete and consistent spacing because they are correlated to the pixel size of the video capture settings. This information was used to choose a time step of 0.03 second and a spatial step size of 1×10^{-4} meters under the structural analysis simulation. The final result of the horizontal force at each given node from a universal axis can be seen in Figure 29.

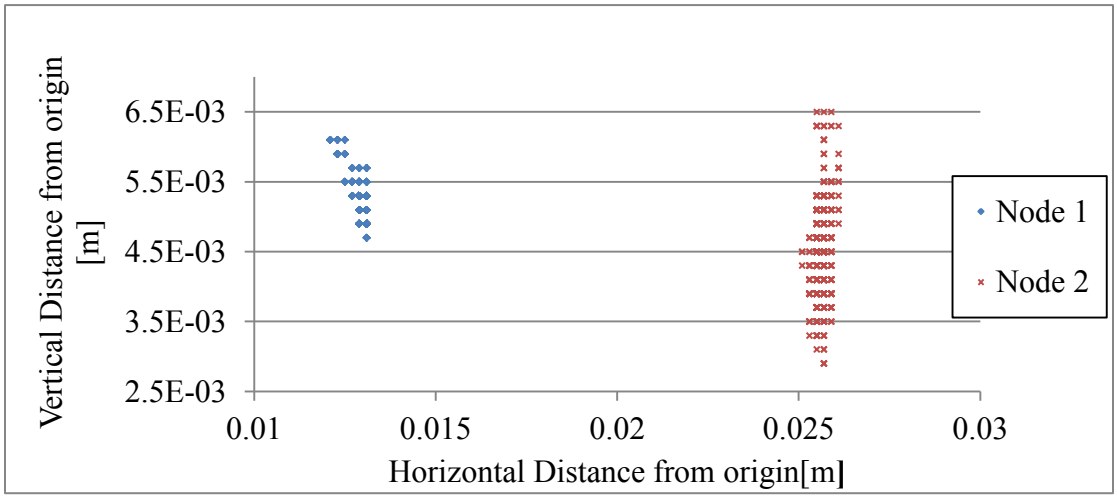

Figure 35: Motion tracked node space domain close-up view on node 1 and 2 in run 1.

Taking a close look at Figure 29 the variability of the force at each node seems to increase due to the larger movements of the nodes extending further from the base node. This might be understood by recognizing that the horizontal force is directly proportional to the drag area. Although nodes further from the base have considerably smaller benthic diameters, they also sweep out at steeper angles relative to the direction of the incoming flow, creating a long rectangular drag force area.

The drag force area was relatively constant for the initial node near the base and maintained a high drag force throughout the experiment. The variations of the initial node were so small that they appear to be non spatially dependent. However, Figure 43 from Appendix 2 shows that there is temporal variation that is on a smaller scale in comparison to the others. The other nodes seem to fall into the domain of highly varying drag forces due to the fluttering effect of the bending algal filament bundles in the fluid flow. The forces in the horizontal direction include the drag force, which is dependent on the node positions, whereas the forces in the vertical direction are based on the volumetric geometry of the link. Because the algal filament bundle link geometry does not change with time, the resultant vertical forces are relatively constant, as can be seen in Figure 36.

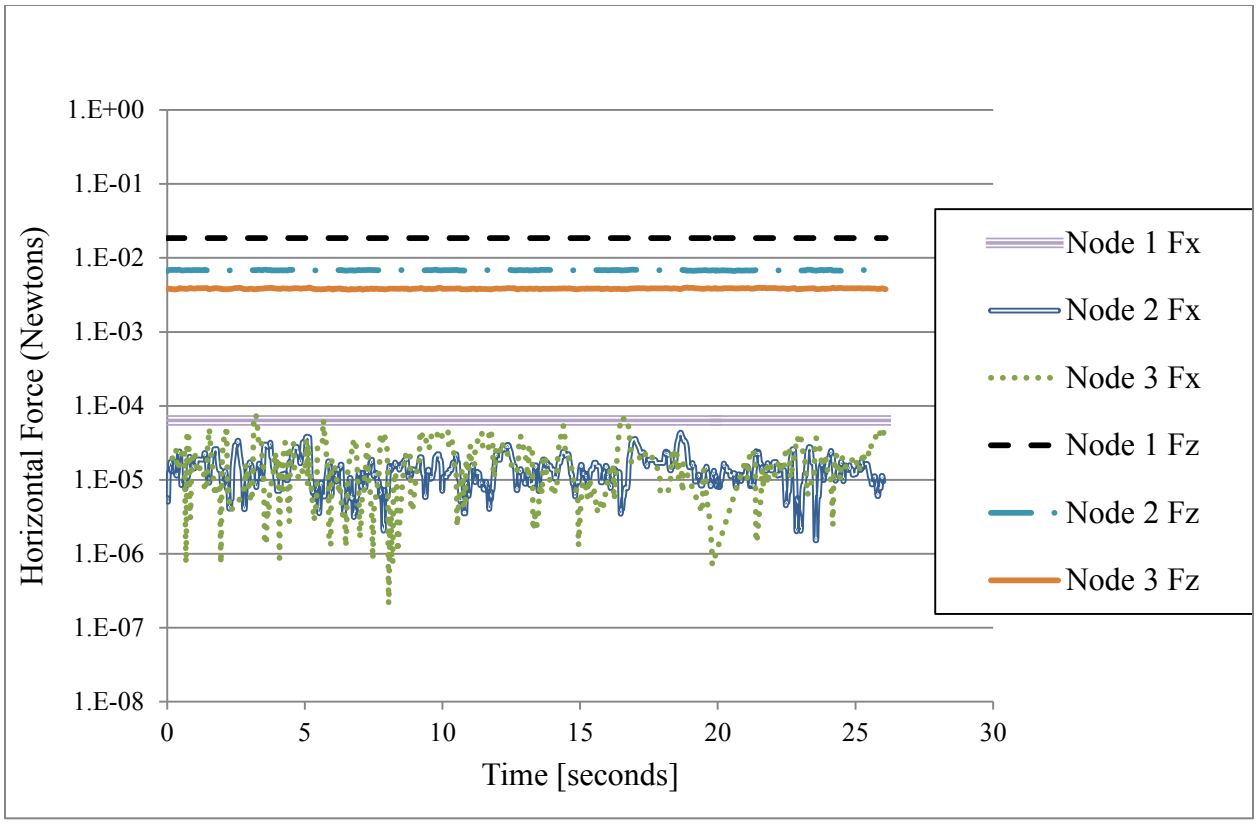

Figure 36: Exerted force results from all nodes in horizontal and vertical directions for run 1.

5.1.2: Analysis of Finite Element Results

In solving the equations for motion for the benthic mass nodes, an assumption was made that the spring and dampener coefficients were the same in the horizontal and vertical direction. This assumption of an isotropic material for the benthic filament might not be true since the cellular arrangement might be arranged to withstand stronger forces in the axial direction; it might not be the mechanical properties of the algal filament but rather the cellular arrangement which might attribute to the successful survival in wave environments (Martone 2007). However, an isotropic assumption was used in this study for computational simplicity.

A key assumption made within the finite element modeling application was that the horizontal and vertical equations of motion could be solved independent from each other. This

assumption might be incorrect from the inference that the horizontal force might induce a bending strain. In this case, there might be some non-linear relationship between the horizontal and vertical forces influencing one another simultaneously. This was not taken into consideration within the mathematical formulation of the finite element modeling of this study and therefore the true parameter of tensile strength might be fundamentally different because the true behavior of the material was not properly taken into account.

The final simulation chosen showed a relatively small difference in error between simulation and observed displacement as shown for node 1 in

Figure 33 and Figure 34; this is probably attributed to the fact that the first node is the most constrained in its range of motion from the universal origin. The maximum tensile strength simulated by the finite element model of the benthic filament bundles was calculated to be 7.63 MPa for the first run under the given flow condition. The subsequent additional runs resulted in an average of 4.2 MPa. While this calculated value seems high considering the observed brittleness of the filaments during handling in experiments, it was in fact within the range of other *Cladophora* studies of tensile strength tests in which a breaking strength in the range of 4-18 MPa was recorded (Johnson, Shivkumar et al. 1996).

6.0: Recommendations

The drag force sub-model can be made more accurate through the separation of pressure drag and form drag for the drag force model, as opposed to lumping it together into a drag force coefficient. Similarly, the determination of hydrodynamic lift can be improved through calculation of the differences in surface pressure due to the pitch of the algal filament bundle in the flow. This can be accomplished by modeling the velocity field passing over the

benthic filaments, which might be handled by more robust programs that can model the hydrodynamic influence on structures. Other finite element methods could be applied besides the basic frame model such as rotational springs at the nodes (Valipour and Bradford 2012) or by assuming a cable model in between each node. The motion tracking technique could be applied in a much more robust way by motion tracking the entire contour of the algal filament bundle and create a flexing truss model that would model the algal filament bundle more precisely and avoid the assumption of isometric homogenous properties.

The way in which the physical properties of the algal filament bundles were estimated was by repeatedly re-running the equations of motion with new values for the spring and dampener constants until the error between the simulation and observed node positions was minimized. There are potential ways to estimate the properties of the structure by using the deformation information directly (Su 2009), however this was not used within this research study.

6.1.1: Advanced Motion Capture Techniques on Algal Filament Bundle

The finite element model was constrained by the method of motion capture, which tracked the movement of the center point of a particular location along the benthic filament bundle. The usage of motion tracking in this study granted the use of finite element modeling based on an assemblage of linear frame components coupled together end to end. However, there might have been other ways to create a more representative simulation of the algal filament structure through elaborate changes in the motion tracking method.

One of the changes in the method of preparing the algal filament bundles for motion tracking would be to stain them with bands across their widths at equal spaced intervals across the length of the filament bundle. The stain should be a distinct color against the benthic filament

and the aquatic background as it would provide an ideal arrangement of distinct colored objects to lock on to the object tracking algorithm. The illustration of the stained method and a close-up perception as might be implemented can be seen in Figure 37.

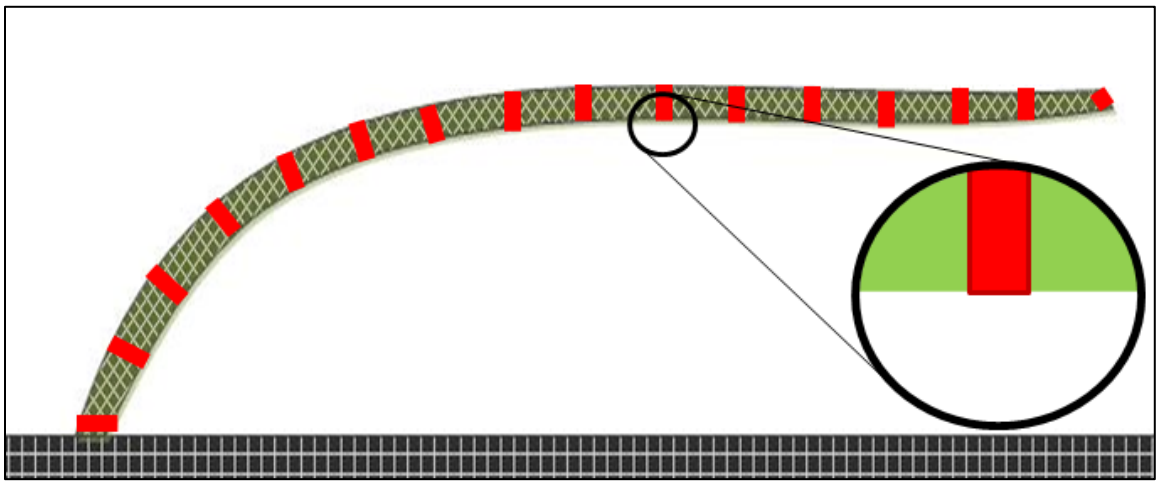

Figure 37: Schematic of advanced staining technique for motion tracking.

Noise in tracking the individual bands of stained segments along the benthic filament bundle could be reduced by implimenting a more robust algorithm for tracking the filament link ends (Ruhnow, Zwicker et al. 2011). The illustration of the staining and a close up can be seen in Figure 38.

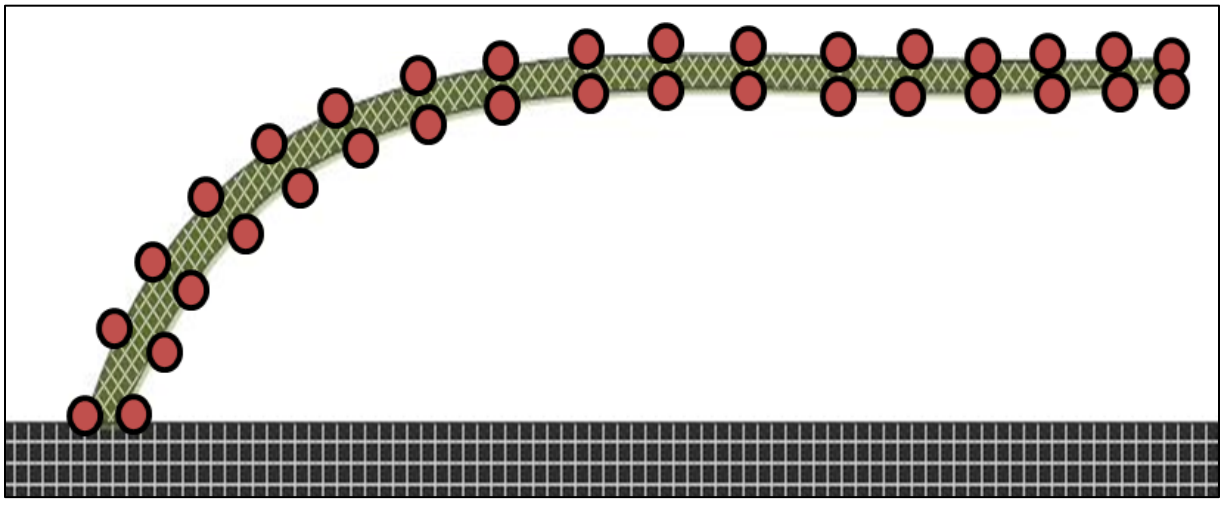

Figure 38: Schematic for concept of motion contour object tracking result on algal filament bundle.

The final product of this new technique can be seen in Figure 39 which would provide a simulation that could capture the properties of tension and compression as the cylindrical structure bends with oncoming flow, as shown in Figure 38. This truss model can provide more detail as to how the material behaves under non-linear two dimensional stress loads.

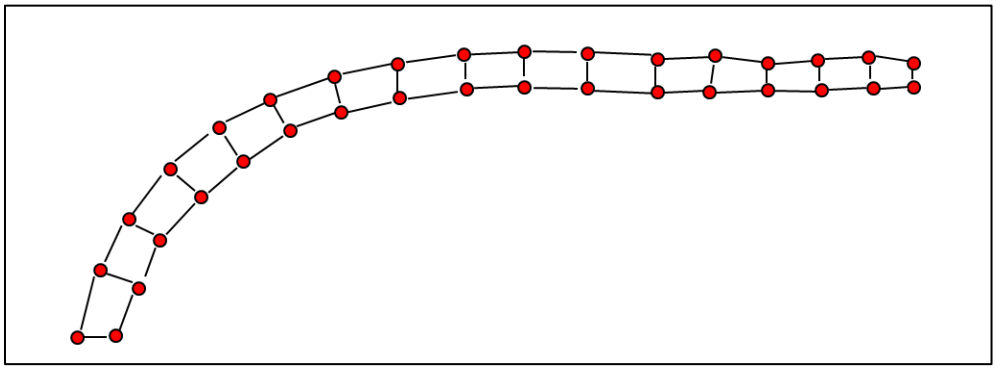

Figure 39: Finite element model simulation concept using contour object tracking technique.

6.1.2: Modeling the Genetic Factor within the Benthic Algal Structural Properties

Whereas the algal filament bundle was treated as merely a structural material in this study, it should be recognized that the algal filament bundle is a living entity. Although filamentous algae are very primitive structurally and contain no complex and higher cognitive abilities as in higher organisms, it cannot be thought of as simply a stagnant material, as the material, structural, and/or morphological properties of the algal community might change in time in response to external paramters as the community compositions shifts (Steinman, Mulholland et al. 1992; Klein and Paschke 2004). Although algae do not have any higher cognitive thinking ability, decision-making strategies occur in essence at the community level when facing changing environmental stressor variables and situations (Domozych and Domozych 2008). Whereas the genetic information within the algal organism enables the initial blueprint for basic functions and

morphology of the algal species, it is the phenetic component which acts as a further decision triggers (Mooi and Gill 2010).

The phenetic component to the organism's genetic material is the ability to turn on and off genes of expression in response to variables that the organism has sensed from the environment.

Table 4: Environmental triggers and internal variables of benthic algae.

Environmental variable triggers		**Internal variables**
• Nutrient Concentration		• Growth Rate
• Fluid Drag Force		• Internal Tensile Strength
• Nutrient Type Availability		• Stipe length
• Wave frequency		• Cellular Arrangement
• Predatory Grazing		• Benthic Filament diameter

An example of how the organism might indirectly make decisions based on environmental triggers can be seen in taking the highly contrasted environmental conditions of two general environmental variables such as fluid flow and nutrient concentration as seen in Table 4. A payoff matrix (Binmore 2007) can be constructed that can provide a probabalistic model for estimating the likelihood of a particular algal growth strategy, given a series of environmental stresser variables, as seen in Table 5. This payoff matrix could be implemented into the next generation of algal growth model to refine prediction of algal growth under different scenarios and over various time-scales (Kim, Jeong et al. 2012).

Table 5: Proposed algal filament bundle decision matrix for nutrient and flow conditions.

	$Q\downarrow$	$Q\uparrow$
$N\downarrow$	$\sigma\downarrow, \mu\downarrow$	$\sigma\uparrow, \mu\downarrow$
$N\uparrow$	$\sigma\downarrow, \mu\uparrow$	$\sigma\uparrow, \mu\uparrow$

- $Q\downarrow$: Low fluid flow condition
- $Q\uparrow$: High fluid flow condition
- $N\downarrow$: Low nutrient condition
- $N\uparrow$: High nutrient condition
- $\sigma\downarrow$: Low filament strength capacity
- $\sigma\uparrow$: High filament strength capacity
- $\mu\downarrow$: Low filament growth rate
- $\mu\uparrow$: High filament growth rate

7.0: Conclusion

The initial motivation for this study was to estimate values of algal filament tensile strength to calibrate a hydrodynamic algal growth model. However this side research project became an interesting struggle which might prove useful in other similar research ventures. Further research of spatial influences of *Cladophora* can divert back to the bigger picture in producing a highly accurate coupled hydrodynamic and filamentous algal growth model. Although the specimen used in this study was *Cladophora*, a similar application could have been done to any number of flexible aquatic organisms which attach to a substrate. The application of the motion tracking can be a useful tool which can provide researchers access to easily investigate the material strength property of similar geometrically flexible organisms in flow. The advantage the proposed method used within this study against is the small amount of monetary resources needed to perform these studies as opposed to a more elaborate and technical methods using custom made highly sensitive stress measuring devices.

The ability to measure the way in which the structure moves at many points simultaneously as opposed to at a local point can also give credit toward the use of finite element

analysis which might provide more in-depth detail as to how the structure deforms from a specified flow field. This ease of use of motion tracking might signify future popular use and therefore motivate the creation of several databases of the structural properties of a wide assortment of biological materials. The structural mechanics application onto a biological material was not common, yet proved to be a useful and insightful tool and might inspire further research to become multi-disciplinary. Additional verification of the method is necessary though application in a range of fluid flow velocities and to filamentous bundles of the same species grown under similar conditions to investigate the differences in the material properties.

The method described in this thesis for estimating the tensile stress in a bundle of attached filamentous algae appears to be successful in developing a reasonable estimate of tensile strength. The work demonstrated the calculation of an averaged internal stress of 4.2 MPa for a bundle of filamentous algae of *Cladophora*, a value consistent with those reported in the literature measured by other means. Overall, however, the methodology is proposed here can take on an open source approach and become more widely used and improved to initiate a database of a wide range of tensile strength values, for a wide range of filamentous structures in flow. The final goal of the project may be useful in studies for prediction of the breaking strength of algal filaments that might inform prediction models for mass sloughing events in nature.

Appendix A: Formal Calculations

1. Formal Proof of Equal Volumes

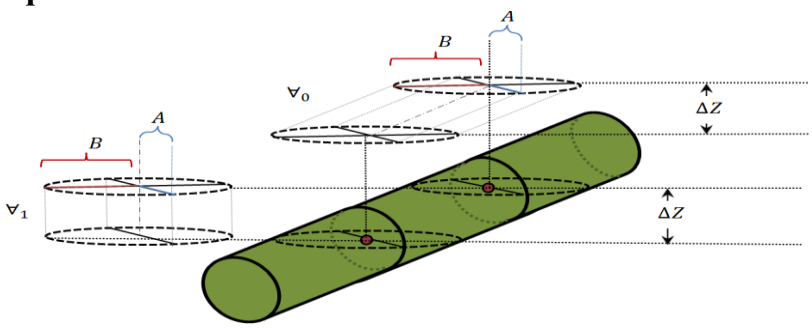

$\forall_1 \doteqdot \forall_0$ *by Cavalieri's Theorem* (Cavalieri and Baroncelli 1987)

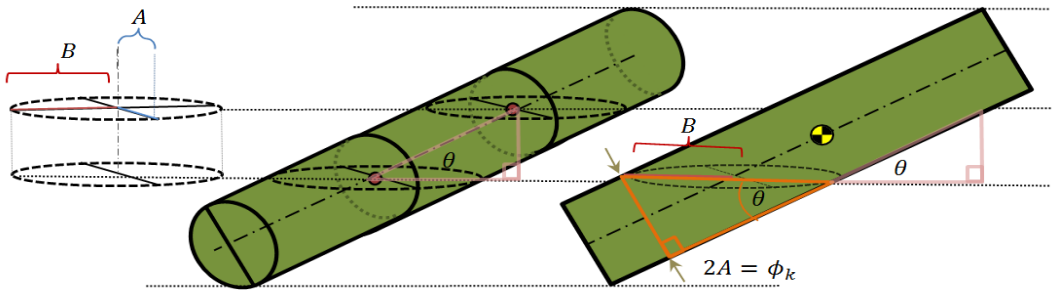

Area of Ellipse cross section

$$Area_{Ellipse} = A_{C_{n_{j-1},[t_i]}} = A \cdot B \cdot \pi$$

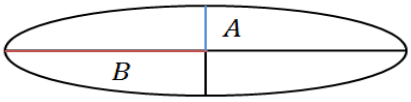

Looking at the orange triangle:

$$A = \frac{\phi_{n_{j-1}}}{2}, \quad B = \frac{\phi_{n_{j-1}}}{2\sin(\theta)} \;\therefore\; Area_{Ellipse} = \overbrace{\left(\frac{\phi_{n_{j-1}}}{2}\right)}^{A} \cdot \overbrace{\left(\frac{\phi_{n_{j-1}}}{2\sin(\theta)}\right)}^{B} \cdot \pi = \boxed{A_{C_{n_{j-1},[t_i]}} = \frac{{\phi_{n_{j-1}}}^2 \pi}{4\sin(\theta)}}$$

$$\forall_{Ellipse\ prism} = \overbrace{\frac{\phi^2\pi}{4\sin(\theta)}}^{Area_{Ellipse}} \cdot \overbrace{(\mathrm{L} \cdot \sin(\theta))}^{\Delta Z} = \boxed{\forall_{Ellipse\ prism} = \frac{\phi^2\pi}{4} \cdot \mathrm{L}}$$

2. Mid-Link Diameter Calculation

When the distance between the nodes is large enough, from each other a truncated cone configuration could be assumed for the volumetric geometry. Since the forces are divided by the midpoint of each link before and after each node, the diameter at the midpoint is of important interest for proper force estimation.

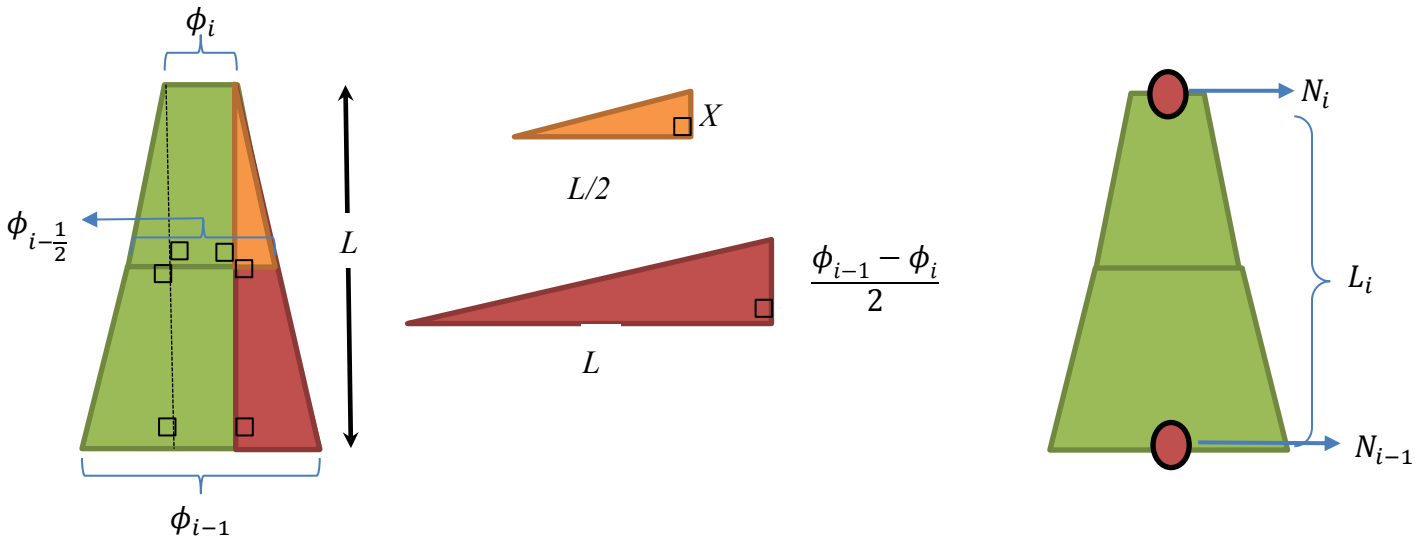

With the use of similar triangles the following proportion can be made:

$$\frac{x}{(L/2)} = \frac{\left(\frac{\phi_{i-1}-\phi_i}{2}\right)}{L}$$

To solve for the unknown length of the segment you may use the property that the diagonal products of the proportional ratios should be equal.

$$x = \left[\left(\frac{\phi_{i-1}-\phi_i}{2}\right)\left(\frac{L}{2}\right)\right]\left(\frac{1}{L}\right) = \frac{\phi_{i-1}-\phi_i}{4}$$

Embedding the previous equation into the following relationship

$$\phi_{i-\frac{1}{2}} = \phi_i + 2x = \phi_i + 2\left(\frac{\phi_{i-1}-\phi_i}{4}\right)$$

$$\boxed{\phi_{i-\frac{1}{2}} = \phi_i + \left(\frac{\phi_{i-1}-\phi_i}{2}\right)}$$

3. Drag Area Calculation for Truncated Cone

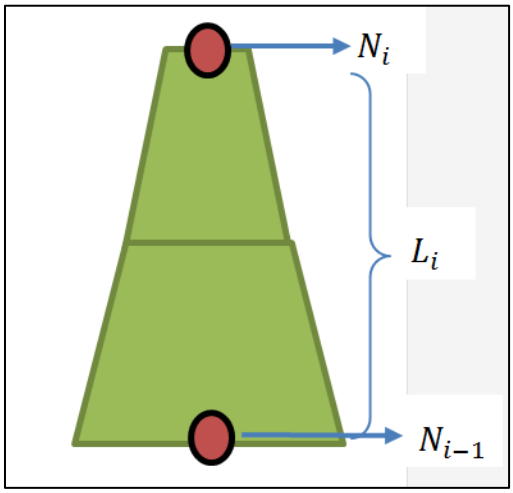

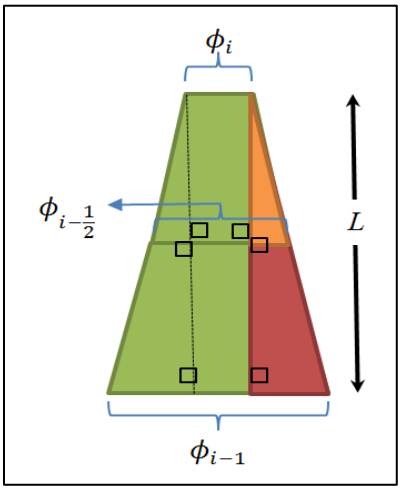

Area of the trapezoidal drag area corresponding to an algal filament bundle node N_j according to the figures above can be seen in the basic equation below

$$A_{D\,j,t_i} = \left(\phi_i + \phi_{i-\frac{1}{2}}\right) * L * \left(\frac{1}{2}\right)$$

The complete drag area equation with all referenced terms can be seen below

$$A_{D\,j,t_i} = \left(\phi_i + \overbrace{\left[\phi_i + \left(\frac{\phi_{i-1} - \phi_i}{2}\right)\right]}^{\phi_{i-\frac{1}{2}}}\right) * \overbrace{\left(z_{[j,t_i]} - z_{[j-1,t_i]}\right)}^{L} * \left(\frac{1}{2}\right)$$

$$\boxed{A_{D\,j,t_i} = \left(\phi_i + \left(\frac{\phi_{i-1} - \phi_i}{4}\right)\right)\left(\frac{\left(z_{[j,t_i]} - z_{[j-1,t_i]}\right)}{2}\right)}$$

4. Truncated Cone Volume Calculation

The volume of the tapered cylinder which begins from the midpoint of the link and ends at the top end of the link can be calculated through the difference of geometric cones.

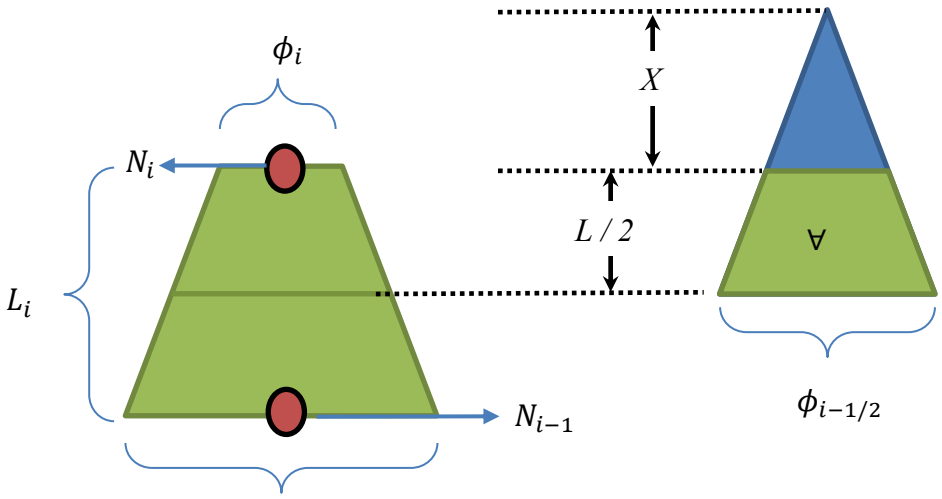

difference of the overall theoretical cone minus the blue cone

$$\forall = \overbrace{\left\{\left[\left(\frac{\pi\phi_{i-1/2}^2}{4}\right) * \left(\frac{L}{2} + X\right)\right] * \frac{1}{3}\right\}}^{Volume\ of\ Large\ Cone} - \overbrace{\left\{\left[\left(\frac{\pi\phi_i^2}{4}\right) * (X)\right] * \frac{1}{3}\right\}}^{Volume\ of\ Smaller\ Cone}$$

To solve for the unknown length of "*X*" one may use the properties of similar triangles to come up with the following equivalent ratios, to solve for *X* in terms of known values.

$$\frac{X}{\phi_i} = \frac{\left(\frac{L}{2} + X\right)}{\phi_{i-1/2}}$$

$$X\phi_{i-1/2} = \phi_i \frac{L}{2} + X\phi_i, \qquad X(\phi_{i-1/2} - \phi_i) = \phi_i \frac{L}{2}, \qquad \boxed{X = \frac{\phi_i(L/2)}{(\phi_{i-1/2} - \phi_i)}}$$

Substituting the length for "*X*" equation into the volume equation can be seen below

$$\boxed{\forall = \left[\left(\frac{\pi\phi_{i-1/2}^2}{4}\right) * \left(\frac{L}{2} + \left[\frac{\phi_i(L/2)}{(\phi_{i-1/2} - \phi_i)}\right]\right)\right] * \frac{1}{3} - \left[\left(\frac{\pi\phi_i^2}{4}\right) * \left[\frac{\phi_i(L/2)}{(\phi_{i-1/2} - \phi_i)}\right]\right] * \frac{1}{3}}$$

5. Bundle Filament Cross Sectional Area Calculations

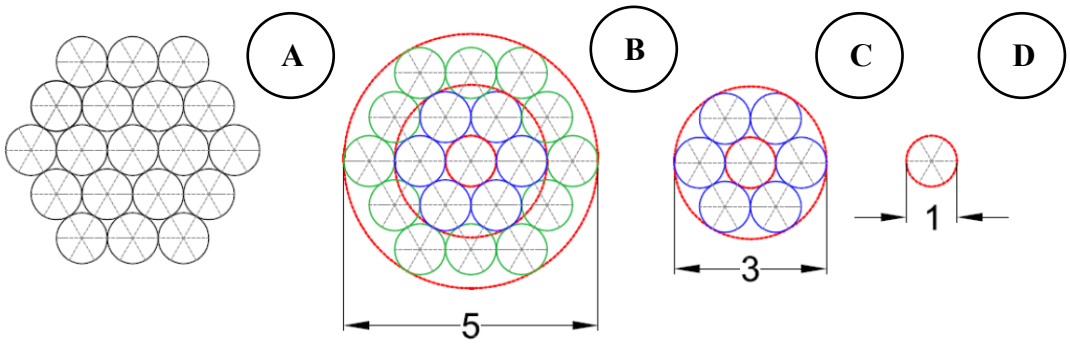

Figure 40: Bundle filament cross sectional area schematic

In Figure 40 image A shows an ideal algal filament bundle where each of the filaments are of equal diameter. The bundle of filaments in Figure 40 image A can be represented by two layers of concentric filament rings as represented in Figure 40 image B (which has an overall outer diameter of five filament diameters). Removing the outer layer from Figure 40 image B results in Figure 40 image C, which is an algal filament bundle with an overall outer diameter length of three individual filament diameters. Figure 40 image D shows a single algal filament diameter with no concentric layers.

To define the distance across the bundle, we use the following definitions:

$$\phi_P = (1+2n)\phi_* \qquad \therefore \qquad n = \left(\frac{\phi_P}{\phi_*} - 1\right)\frac{1}{2} \quad \ni \quad [n \in \mathbb{N}]$$

where ϕ_P is the measured dried bundle filament diameter [m], n is an integer number of concentric ring layers, where a single algal filament is layer zero [ ], ϕ_* is the diameter of a single algal filament [m], $\mathbb{N}$ is the domain of natural numbers which are positive integers greater than zero.

A relationship between the number of concentric layers and total number of circles can be seen in the following relationship:

$$N = 1 + \sum_{i=0}^{n} 6i\,, \qquad A = \left(\frac{\pi\phi_*^2}{4}\right) * N$$

Where N is the total number of algal filaments found in the bundle [ ], and A_{bc} is the overall cross sectional area of each of the algal filaments in the bundle [m]

$$A_{bc} = \left(\frac{\pi\phi_*^2}{4}\right) * \left[1 + \sum_{i=0}^{q} 6i\right] \quad such\ that: q = \left(\frac{\phi_P}{\phi_*} - 1\right)\frac{1}{2} \quad \ni \quad [n \in \mathbb{N}]$$

6. Solving for Internal Force from Dampener and Spring Coefficients

Using the force function from node n_{j-1} and time t_i from Equation (14), one can solve for the damping coefficient in terms of the spring coefficient.

$$F_{x_{n_{j-1,[t_i]}}} = x_{n_{j-1,[t_i]}} k_{n_{j-1}} + \dot{x}_{n_{j-1,[t_i]}} c_{n_{j-1}} + \ddot{x}_{n_{j-1,[t_i]}} m_{n_{j-1}}$$

$$c_{n_{j-1}} = \left(F_{x_{n_{j-1,[t_i]}}} - x_{n_{j-1,[t_i]}} k_{n_{j-1}} - \ddot{x}_{n_{j-1,[t_i]}} m_{n_{j-1}}\right) / \dot{x}_{n_{j-1,[t_i]}}$$

Using the equations of motion from node n_{j-1} and time t_{i+1} we can solve for the spring coefficient in terms of the damping coefficient.

$$F_{x_{n_{j-1,[t_{i+1}]}}} = x_{n_{j-1,[t_{i+1}]}} k_{n_{j-1}} + \dot{x}_{n_{j-1,[t_{i+1}]}} c_{n_{j-1}} + \ddot{x}_{n_{j-1,[t_{i+1}]}} m_{n_{j-1}}$$

$$k_{n_{j-1}} = \left(F_{x_{n_{j-1,[t_{i+1}]}}} - \dot{x}_{n_{j-1,[t_{i+1}]}} c_{n_{j-1}} - \ddot{x}_{n_{j-1,[t_{i+1}]}} m_{n_{j-1}}\right) / x_{n_{j-1,[t_{i+1}]}}$$

Substituting the equation for the spring coefficient in terms of the damping coefficient at time t_{i+1} into the equation of the damping coefficient in terms of the spring coefficient at time t_i, one may solve for the damping coefficient.

$$c_{n_{j-1}} = \frac{\left(\frac{F_{x_{n_{j-1,[t_i]}}}}{\dot{x}_{n_{j-1,[t_i]}}} - \frac{F_{x_{n_{j-1,[t_{i+1}]}}} x_{n_{j-1,[t_i]}}}{x_{n_{j-1,[t_{i+1}]}} \dot{x}_{n_{j-1,[t_i]}}} + \frac{\ddot{x}_{n_{j-1,[t_{i+1}]}} m_{n_{j-1}} x_{n_{j-1,[t_i]}}}{x_{n_{j-1,[t_{i+1}]}} \dot{x}_{n_{j-1,[t_i]}}} - \frac{\ddot{x}_{n_{j-1,[t_i]}} m_{n_{j-1}}}{\dot{x}_{n_{j-1,[t_i]}}}\right)}{\left(1 - \frac{\dot{x}_{n_{j-1,[t_{i+1}]}} x_{n_{j-1,[t_i]}}}{x_{n_{j-1,[t_{i+1}]}} \dot{x}_{n_{j-1,[t_i]}}}\right)}$$

Substituting the equation for the damping coefficient for node n_{j-1} back into the spring coefficient at node n_{j-1}. Solving for all of the internal forces at each node for N nodes at a specific time t_i can be solved using the resulting equation (Chopra 2001).

$$k_{n_{j-1}}\begin{bmatrix} 2 & -1 & 0 & \dots \\ -1 & 2 & -1 & 0 \\ 0 & -1 & \ddots & -1 \\ \vdots & 0 & -1 & 2 \end{bmatrix}\begin{bmatrix} x_{n_{j-1,[t_i]}} - x_{n_{j-1,[t_{i-1}]}} \\ x_{n_{j,[t_i]}} - x_{n_{j,[t_{i-1}]}} \\ \vdots \\ x_{n_{N,[t_i]}} - x_{n_{N-1,[t_{i-1}]}} \end{bmatrix} = \begin{bmatrix} F_{\sigma_{n_{j-1}},[t_i]} \\ F_{\sigma_{n_j},[t_i]} \\ \vdots \\ F_{\sigma_{n_N},[t_i]} \end{bmatrix}$$

Appendix B: Experimental Measurements

1. Experimental Run 1: Algal filament bundle measurements

Table 6: Run 1: Wet algal filament bundle measurements

Node No.	Diameter (m)	Link no.	Length (m)
0	0.025	1	0.03
1	0.0125	2	0.029
2	0.01	3	0.031
3	0.0075	4	0.0175
4	0.005		

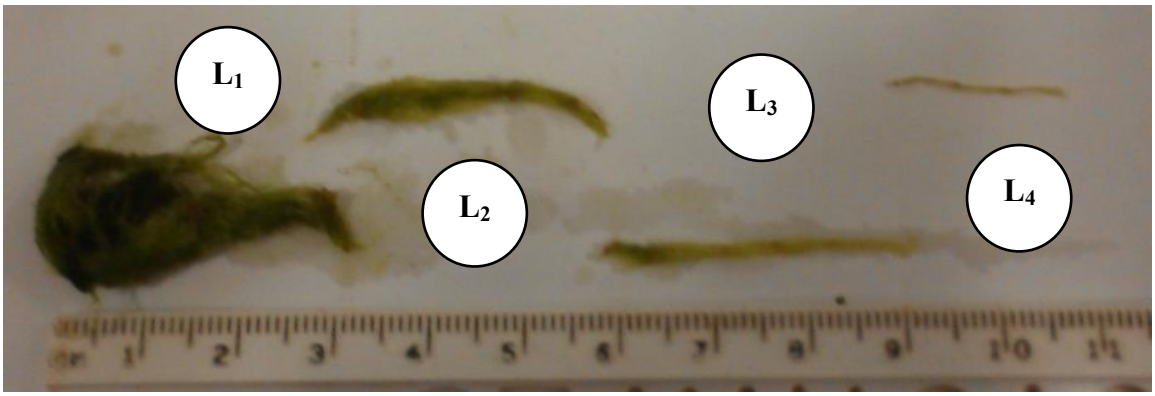

Figure 41: Algal filament bundle cut at measured nodes
Note: The centimeter ruler is placed in the picture for scale

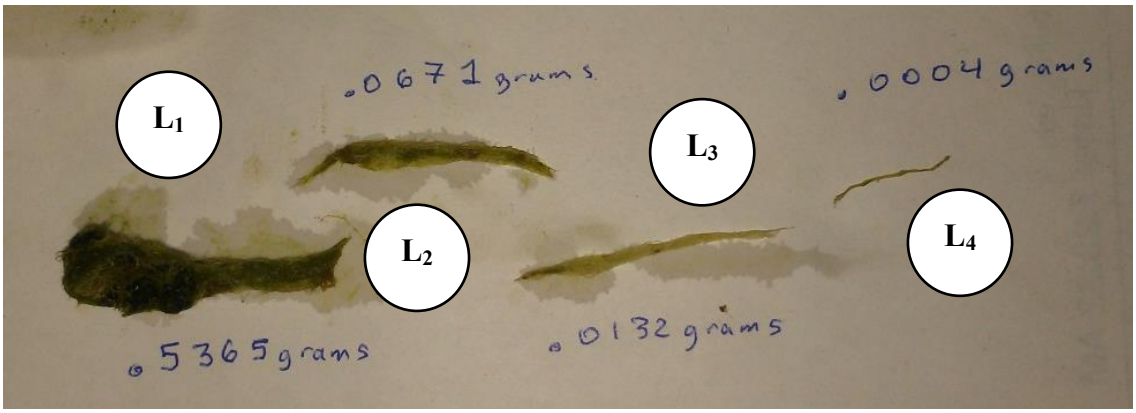

Figure 42: Algal filament bundle mass wet weight measurements per link

2. Horizontal Force vs. Time Graphs for Individual Nodes

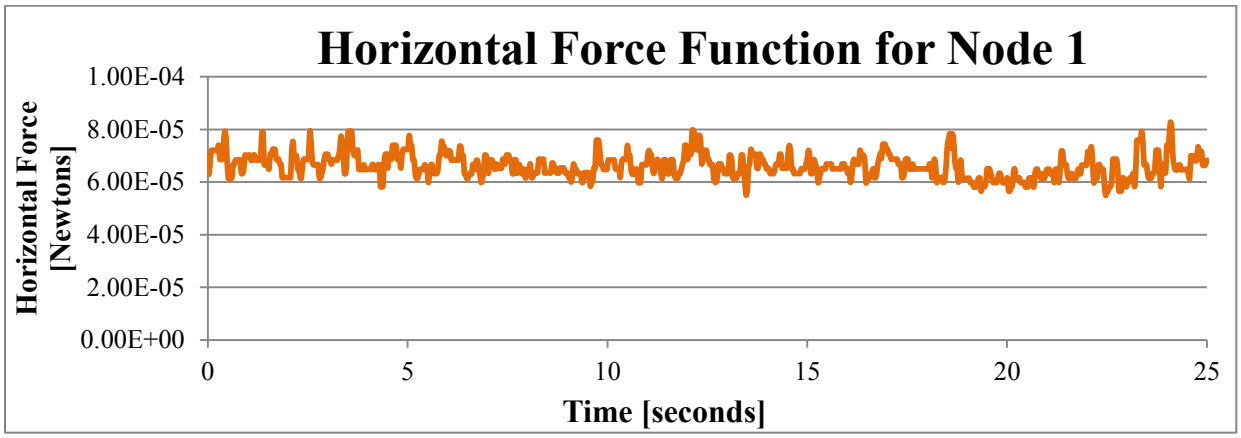

Figure 43: Node 1: Horizontal force vs. time

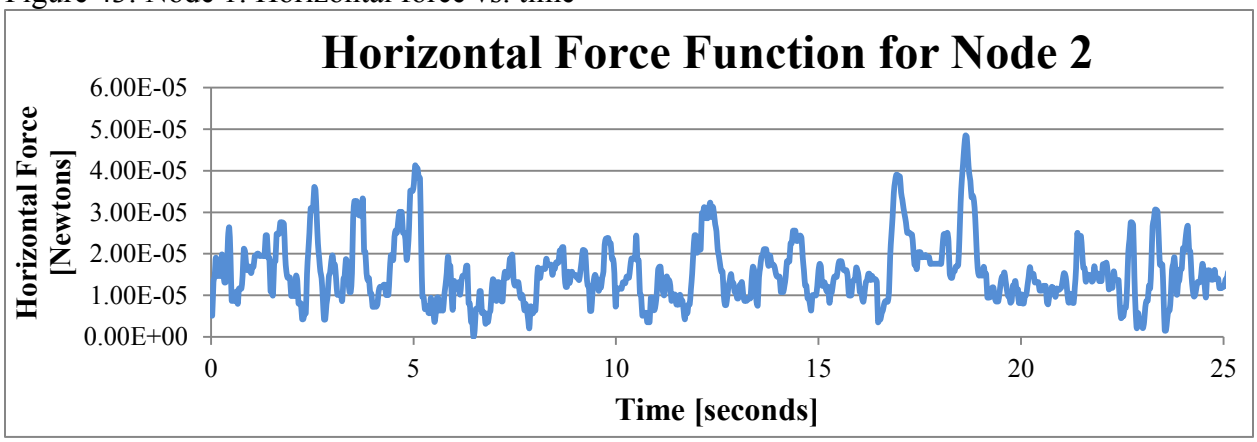

Figure 44: Node 2: Horizontal force vs. time

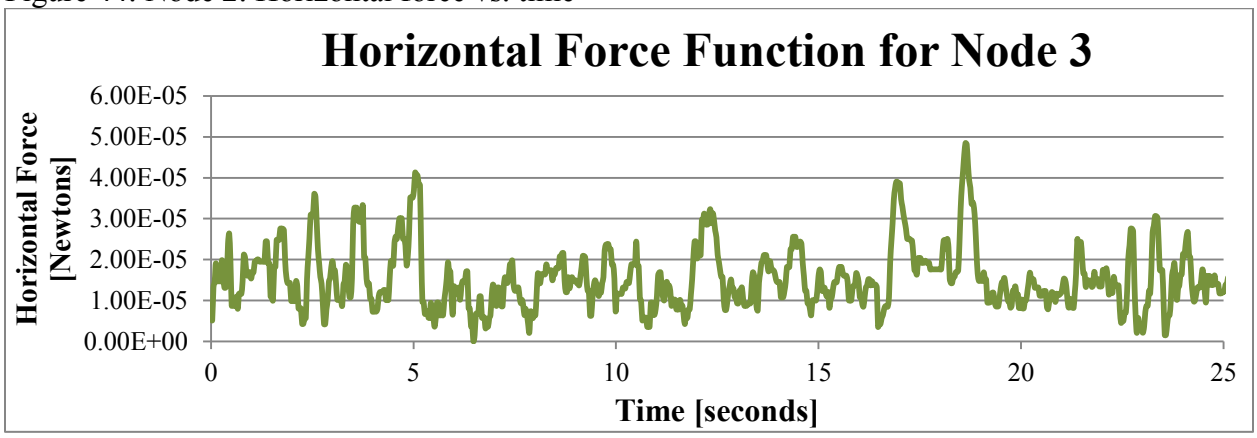

Figure 45: Node 3: Horizontal force vs. time

3. Vertical Force vs. Time Graphs for Individual Nodes

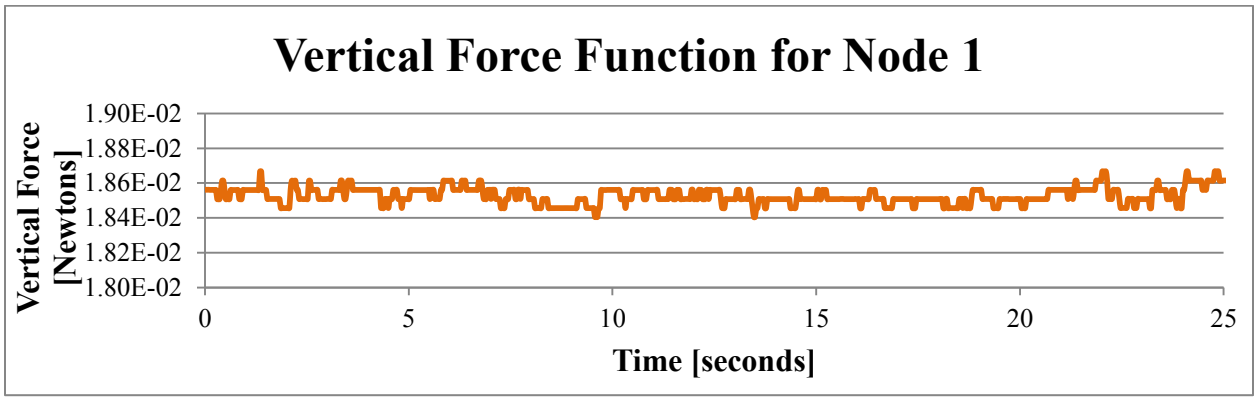

Figure 46: Node 1: Vertical force vs. time graph

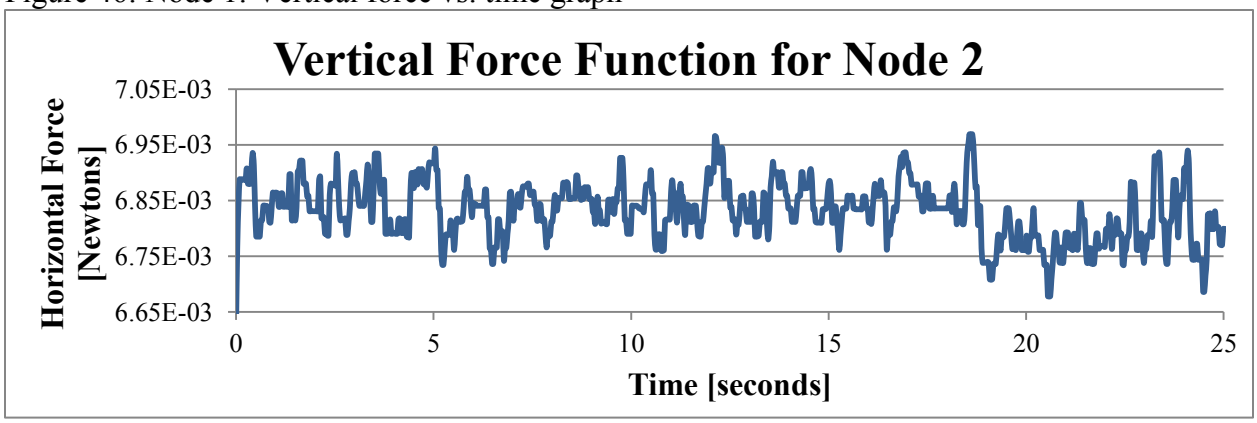

Figure 47: Node 2: Vertical force vs. time graph

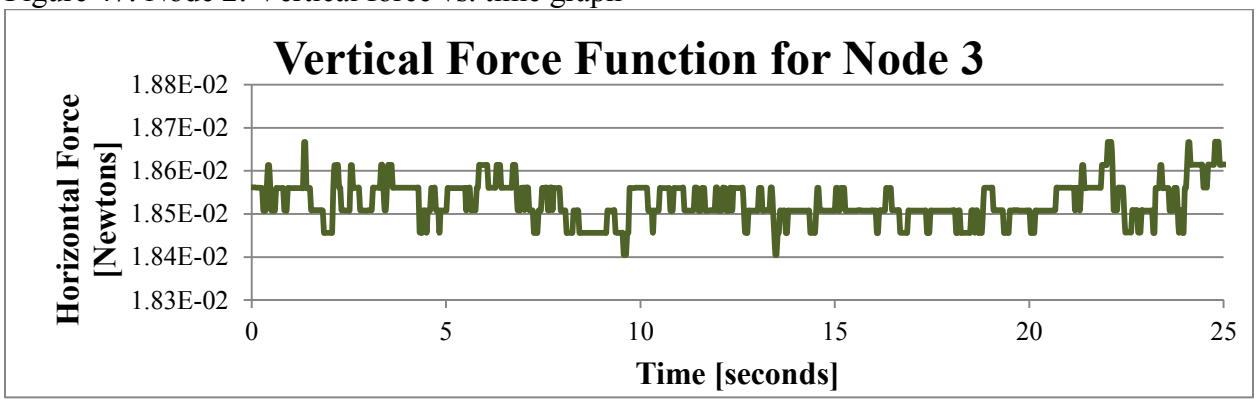

Figure 48: Node 3: Vertical force vs. time graph

Appendix C: Future Research Work

1. Benthic Filamentous Algae Model Application

Filamentous algal growth models are helpful for prediction purposes in a wide range of situations where filamentous algal growth is desired. Such situations can be in an industrial setting (Bernard 2011) or in a natural system, and a growth model can serve as a tool to make informed decisions on what can be done to achieve or maintain a desired state of filamentous algae in the field (Delrue, Seiter et al. 2012). Many current algal growth models are based on simple, linear, time-dependent differential equations that predict growth within a narrow range of tolerance scaled to the small lab bench scale (Kannel, Kanel et al. 2011). Most benthic algal growth models are based on the efficiency of resource utilization by the algae organism (Auer, Tomlinson et al. 2010). There are plenty of well-established and successful algal growth models that predict behavior within acceptable ranges on the small scale. However, there will be a continued movement to achieve equal rates of predicted growth on larger scale scenarios (Quinn, de Winter et al. 2011).

The first initial growth models were based on chemostat (well mixed batch reactor) studies where parameters of interest were primarily driven by chemical or biological elements (Westerhoff, Hu et al. 2010). Early algal growth models were constructed using internal biological mechanisms of the algal species as parameters (Raaijmakers 1987) and were modeled on the basis of metabolic efficiency (Grover, Sterner et al. 1999), or the concept of a "cell quota" (Cherif and Loreau 2010). Using these ideas of biological growth, successful models have been implemented for use on small scale, such as a stream (Ambrose, Martin et al. 2006), or on a larger scale, such as for an entire region or watershed (Djodjic, Montas et al. 2002). Despite these advances, there will be a continued effort to make algal models more complex and accurate

in an attempt to understand and predict the behavior of filamentous algae across scales. The next generation of algal growth models will incorporate much more spatial information to limit the loss of accuracy as the scale of analysis increases.

On larger scales, the predicted values of chemostat models are conservative and typically deviate from reality when applied to benthic cultivation systems (Carpenter 1989). The reason for this occurrence is that on a small scale, it is appropriate to ignore spatially-dependent processes such as the rate of nutrient diffusion. However, this key assumption adds uncertainty into the model for larger scales because external physical transport processes become predominant (Ferreira, Andersen et al. 2011). Improved models would develop the connection between effects of the external environment and the growth of the filamentous algae to predict the production and loss rate of benthic biomass (Rasmussen, Petersen et al. 2009). Through manipulation of external environmental parameters, new algal growth models could provide the opportunity to optimize algal growth for a particular flow condition (Donaghay and Osborn 1997). Past studies have attempted to model these dynamics.

2. Proposed Coupled Algal Growth and Hydrodynamic Model

There are several elements of the external aquatic environment that directly affect the growth state of an attached filamentous algal organism (Koehl and Rosenfeld 2006). To adequately account for these elements, a number of sub models might be proposed to address particular dynamics. Some proposed sub models that describe conditions that affect algal growth can be seen in Table 7. Development of many of these models of external factors requires bridging multiple disciplines together (Nikora 2010), and the coupling of these distinct sub-models can create an integrative model of benthic algae, which can simultaneously simulate several aspects of physical and biological behavior. All of the proposed models in Table 7 add elements of spatial processes that can affect the growth (A, D) or removal (B, C) of the benthic algal filament.

Table 7: Proposed hydrodynamic sub-models for filamentous algal growth.

Proposed Sub-model		**Brief Description of Proposed Sub-Model**
A	Mass Transfer Model (**MTM**)	Algal filaments can be limited by the nutrient influx rate from the surrounding fluid due to turbulent mixing and mass diffusion.
	References: (Larned, Nikora et al. 2004), (Kuhl, Glud et al. 1996), (Hondzo, Feyaerts et al. 2005)	
B	Benthic Algal Sloughing Model (**BASM**)	Mechanistic removal of benthic filamentous algae due to shear stresses from oncoming flow.
	References: (Hondzo and Wang 2002), (Biggs and Thomsen 1995), (Koehl 1999)	
C	Dense Overshadowing Growth Model for Algal Sloughing (**DOGMAS**)	During high dense growth in attached algal growth systems, biological failure can occur in the lower canopy due to light limitation inducing sloughing.
	References: (Higgins, Hecky et al. 2008)	
D	Planar Area Light Exposure Rate Model (**PALERM**)	Benthic algal surface areal exposure rate to the oncoming light source governed by the aquatic wave frequency.
	References: (Pedersen, Nejrup et al. 2012), (Wallin, Qvarfordt et al. 2011), (Carpenter 2007)	

A preliminary research endeavor involved the integration of two specific sub-models into a conventional algal growth model to show the effect of hydrodynamics on a benthic algal system as seen in Figure 49. The first sub-model in question was the MTM (Mass Transfer Model) which involves the nutrient diffusion rate dictated by the boundary layer thickness around the benthic filaments. The other sub-model is the BASM which models benthic sloughing of algae due to fluid shearing. Benthic algal sloughing could be attributed to biological, spatial, or structural sources (Flindt, Pedersen et al. 2007).

The biological sources of sloughing could be due to nutrient deficiencies causing a structural weakness in the benthic stalks (Rier and Stevenson 2006). A spatial element may include taller stalks overshadowing the lower canopy benthic stalks as mentioned in section C of Table 7. The reasoning behind sloughing in the proposed DOGMAS model is where a dense growth condition provides less light traveling to the lower canopy. This will eventually cause the lower canopy portions of the benthic filament to become weak enough to shear with the incident flow (Higgins, Hecky et al. 2008). Another possible source of a sloughing event, which will be the primary focus of this thesis, is modeling the effect of the fluid force on the strength of the benthic filament. To investigate the effects of fluid shearing on an algal filament, there is an assumption that any sloughing is predominantly influenced by mechanistic limitations of the benthic algae.

During the early phases of this study, an attempt was made to integrate the first two sub-models from Table 7 into an algal growth model. Sub-models (A) entitled Mass Transfer Model (MTM) and (B) Benthic Algal Sloughing Model (BASM) can be implemented together into a growth model, as seen in Figure 49. This diagram also shows that a hydrodynamic simulation of the system can be accomplished through the use of a computational fluid dynamics

model (CFDM). The physical model (PM) can serve as a basis for reference and model validation for the individual (CFDM), (MTM), and (BASM) sub-models. The combination of the positive (MTM) and negative (BASM) models into the algal growth model can involve the spatial integration onto a two dimensional surface as an integrated benthic algal model (IBAM).

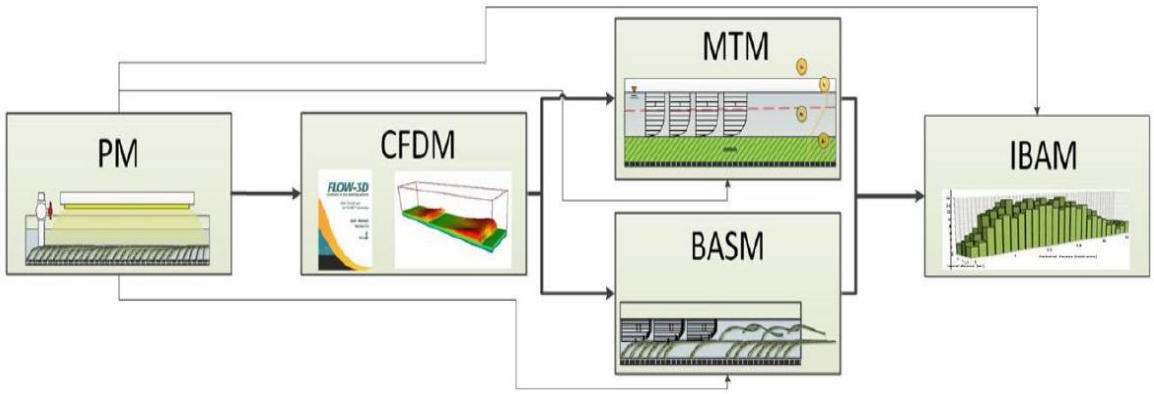

Model Acronym	Acronym Description
PM	Physical Model
CFDM	Computational Fluid Dynamics Model
MTM	Benthic Algal Sloughing Model
BASM	Benthic Algal Sloughing Model
IBAM	Integrated Benthic Algae Model

Notes:
- Arrows represent the pathways of information between models
- Dark lines indicate direct model input
- Thin lines indicate reference or data validation

Figure 49: Proposed hydrodynamics integration into algal model.

One of the more difficult aspects within a mechanistic sloughing model (BASM) is estimating the structural properties of the algal filament. One of the many obstacles in establishing a model for the structural property of an algal filament derives from the technical hurdles faced when measuring the internal forces of the filament. Within the field of structural mechanics, the devices used for measuring the internal properties of a material are designed for substances with considerably higher strength than the comparatively weak properties of algal filaments. There are methods to estimate the tensile forces of an algal filament that use specialized tensile testing (Johnson, Shivkumar et al. 1996) or involve the use of custom made equipment (Boller and Carrington 2006; Fonseca, Koehl et al. 2007). Within this study, an alternative method was devised using fluid force concepts to estimate tensile forces by utilizing readily available equipment.

3. Potential feedback Application to Algal Modeling

For industrial applications, where optimized growth and production of the benthic filamentous algae is the aim, one possible method of optimization could be through the use of bio-monitoring (Cerveny, Setlik et al. 2009) and feedback (Csavina, Stuart et al. 2011). An illustration of this concept can be seen in Figure 50, which shows a control feedback system optimizing a series of filamentous algal bioreactors from the use of internal algorithms, which have control over the operations of the system. The use of autonomous monitoring is a new venue that can help with the economics of operation due to the large scale of the industrial photo-bioreactor (Bernard 2011).

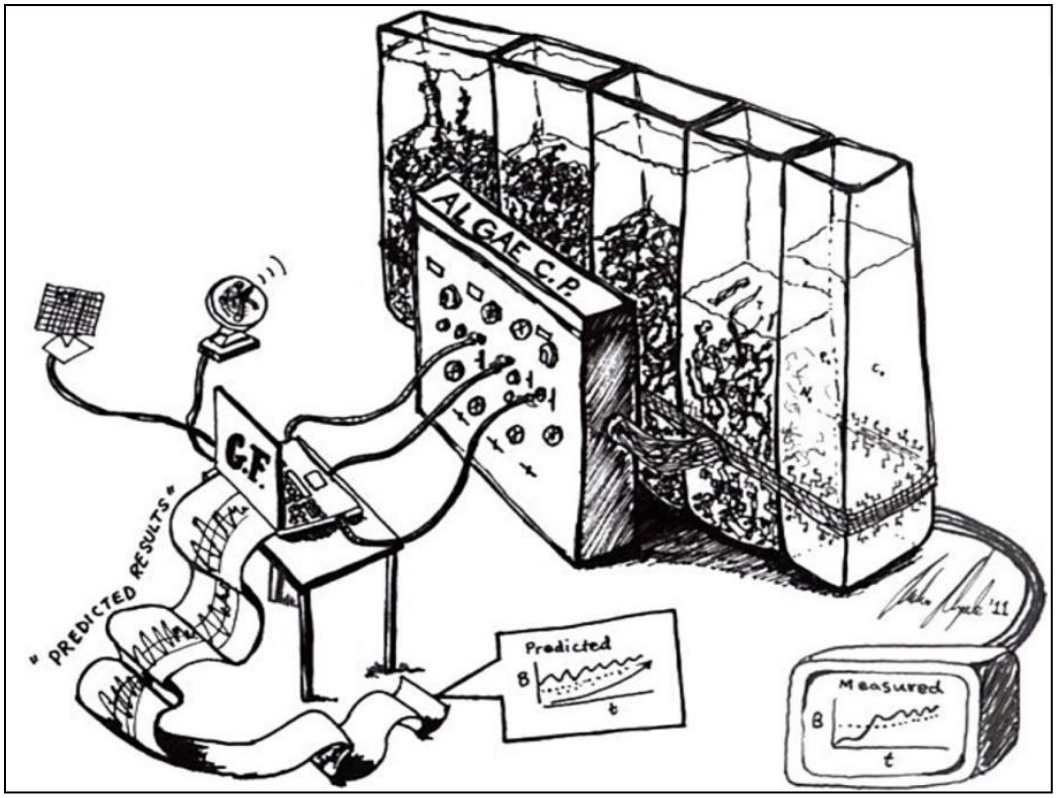

Figure 50: Coupled hydrodynamic and algal growth model illustration concept.
On the Laptop Panel: "G.F" stands for a "Green Flow" a theoretical software platform. In front of the five algal tanks is a control system labeled "Algae C.P." for Algae Control Panel

A feedback control system can receive information on how the algal community is performing (Guedri and Durrieu 2008) and cross check the sensor measured data against the predicted algorithm growth (Sanchez, Berenguel et al. 2003). These next generations of algorithms that are being implemented in feedback control systems can provide consistent optimization autonomously throughout the design life of the industrial system (Briassoulis, Panagakis et al. 2010). However, this creates a need for highly accurate and high resolution algal growth models to effectively implement feedback-monitoring control systems to be cost effective. From an operations standpoint, autonomous maintenance of the bioreactor could be controlled in part through simple means of the hydrodynamic manipulation of the system, thus

providing a type of adaptive hydrodynamic system according to the state of the predicted algal biomass.

From an economic standpoint, if the electrical cost outweighs the predicted productivity outcome, the pumping rate could be adjusted to reduce unnecessary cost. One such scenario in which an adaptive hydrodynamic system might work is during the initial high growth phase of an algal population. The high nutrient demand should be satisfied with a high flow rate to ensure proper nutrient mixing. During dense growth periods, the high pumping rate might cause excessive sloughing and should be lowered to maximize the steady-state algal biomass. The benthic algae population could even be steered towards a specific desired morphology through the influence of hydrodynamics. This affects the phenotypic qualities of the organism over time and impacts filament length or filament branching behavior (Martone and Denny 2008).

4. Long Term Parameter Derivation by Time Lapsed Motion Tracking

All of the experiments were made by employing algal filament bundles that were harvested during arbitrary points in their state of growth. An important element to this study would be to quantify the rate of change of morphology of the benthic filament bundle over time. The algal filament bundle might have parameters which cannot be measured in real time and can only be observed over a longer period such as those listed in Table 8. To estimate parameters that would require a longer span of time for proper measurement, a time lapse video capture approach could be used. The primary reason for using a time-lapse video can be to reduce the amount of video data an analysis program would have to use to extract fundamental data from the time

varying feature in the footage. The time-lapse video can also be a very good tool to observe various phenomena such as the dense growth behavior and periodic sloughing events which would be very hard to witness in real-time observation.

Table 8: List of long-term algal filament bundle parameters of interest

Name of Parameter of Interest	**Parameter Description**
Algal filament bundle growth rate	How fast the algal filament bundle grows in the axial direction
Filament Bundle diameter growth	Diameter growth rate from the axial center of bundled node
Biofilm thickness height	Treating the algal filament bundles in unison as a biofilm layer
Bulk fluid depth	Height of the aquatic water surface in reference to benthic filament canopy

The time-lapse implementation merely involved an extra step in the motion capture video analysis used in this study, where instead of using direct video footage of the experiment, individual snapshots would be compiled together to create the video footage that would then be embedded into the motion tracking program as seen Figure 51.

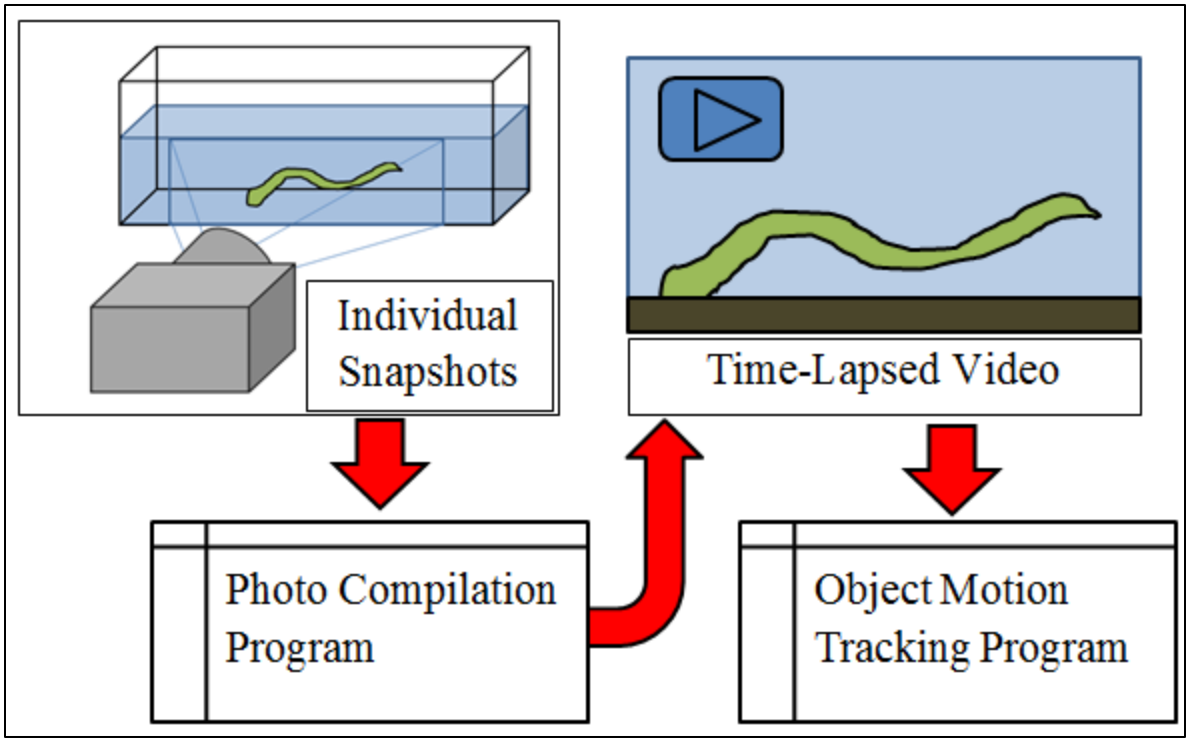

Figure 51: Time-lapse video compiling procedure concept.

Once the time lapsed video was input, the motion tracking program take a measurement every 30 milliseconds using standard video formats for the time-lapsed video. The measurement interval of the data log program can be converted back to real time through the example conversion presented in Equation (25).

$$\overbrace{30\ milliseconds_{video}}^{Data\ Recording\ Interval}\left(\frac{1\ second_{video}}{1000\ millisecond_{video}}\right)\overbrace{\left(\frac{30\ frames}{1\ second_{video}}\right)}^{Frame\ Rate}\overbrace{\left(\frac{10\ minutes_{real}}{1 frame}\right)}^{Time\ Lapse} \quad (25)$$

Bibliography

Adey, W. H., P. C. Kangas, et al. (2011). "Algal Turf Scrubbing: Cleaning Surface Waters with Solar Energy while Producing a Biofuel." BioScience **61**(6): 434-441.

Adey, W. H. and K. Loveland (2007). Dynamic aquaria : building and restoring living ecosystems. Amsterdam ; Boston, Academic Press.

Ambrose, J. R. B., J. L. Martin, et al. (2006). WASP7 benthic algae - model theory and user's guide supplement to water quality analysis simulation program (WASP) user documentation. Washington, DC, U.S. Environmental Protection Agency, Office of Research and Development**:** v, 26 p.

Astbury, W. T. and R. D. Preston (1940). "The Structure of the Cell Wall in Some Species of the Filamentous Green Alga Cladophora." Proceedings of the Royal Society of London. Series B, Biological Sciences **129**(854): 54-76.

Auer, M. T., L. M. Tomlinson, et al. (2010). "Great Lakes Cladophora in the 21st Century: Same Algae-Different Ecosystem." Journal of Great Lakes Research **36**(2): 248-255.

Bathe, K.-J. r. (1982). Finite element procedures in engineering analysis. Englewood Cliffs, N.J., Prentice-Hall.

Bernard, O. (2011). "Hurdles and challenges for modelling and control of microalgae for CO2 mitigation and biofuel production." Journal of Process Control **21**(10): 1378-1389.

Bhat, K., S. Seitz, et al. (2002). Computing the Physical Parameters of Rigid-Body Motion from Video

Computer Vision — ECCV 2002. A. Heyden, G. Sparr, M. Nielsen and P. Johansen, Springer Berlin / Heidelberg. **2350:** 551-565.

Biggs, B. J. F. and H. A. Thomsen (1995). "DISTURBANCE OF STREAM PERIPHYTON BY PERTURBATIONS IN SHEAR-STRESS - TIME TO STRUCTURAL FAILURE AND DIFFERENCES IN COMMUNITY RESISTANCE." Journal of Phycology **31**(2): 233-241.

Binmore, K. G. (2007). Playing for real : a text on game theory. Oxford ; New York, Oxford University Press.

Boller, M. L. and E. Carrington (2006). "In situ measurements of hydrodynamic forces imposed on Chondrus crispus Stackhouse." Journal of Experimental Marine Biology and Ecology **337**(2): 159-170.

Briassoulis, D., P. Panagakis, et al. (2010). "An experimental helical-tubular photobioreactor for continuous production of Nannochloropsis sp." Bioresource Technology **101**(17): 6768-6777.

Bruss, I. R. and G. M. Grason (2012). "Non-Euclidean geometry of twisted filament bundle packing." Proceedings of the National Academy of Sciences of the United States of America **109**(27): 10781-10786.

Carpenter, R. C. (2007). "Mass transfer limitation of photosynthesis of coral reef algal turfs." Marine Biology: 16.

Carpenter, S. R. (1989). "Temporal variance in lake communities: blue-green algae and the trophic cascade." Landscape Ecology **3**(3-4): 175-184.

Cavalieri, B. and G. Baroncelli (1987). Carteggio. Firenze, L.S. Olschki.

Cerveny, J., I. Setlik, et al. (2009). "Photobioreactor for cultivation and real-time, in-situ measurement of O-2 and CO2 exchange rates, growth dynamics, and of chlorophyll fluorescence emission of photoautotrophic microorganisms." Engineering in Life Sciences **9**(3): 247-253.

Cherif, M. and M. Loreau (2010). "Towards a more biologically realistic use of Droop's equations to model growth under multiple nutrient limitation." Oikos **119**(6): 897-907.

Chopra, A. K. (2001). Dynamics of structures : theory and applications to earthquake engineering. Upper Saddle River, NJ, Prentice Hall.

Csavina, J. L., B. J. Stuart, et al. (2011). "Growth optimization of algae for biodiesel production." Journal of Applied Microbiology **111**(2): 312-318.

Delrue, F., P. A. Seiter, et al. (2012). "An economic, sustainability, and energetic model of biodiesel production from microalgae." Bioresource Technology **111**: 191-200.

Denny, M. W. and B. B. Hale (2003). "Cyberkelp: an integrative approach to the modelling of flexible organisms." Philosophical Transactions of the Royal Society of London Series B-Biological Sciences **358**(1437): 1535-1542.

Depew, D. C., A. J. Houben, et al. (2011). "Distribution of nuisance Cladophora in the lower Great Lakes: Patterns with land use, near shore water quality and dreissenid abundance." Journal of Great Lakes Research **37**(4): 656-671.

Djodjic, F., H. Montas, et al. (2002). "A decision support system for phosphorus management at a watershed scale." Journal of Environmental Quality **31**(3): 937-945.

Domozych, D. S. and C. R. Domozych (2008). "Desmids and Biofilms of Freshwater Wetlands: Development and Microarchitecture." Microbial Ecology **55**(1): 81-93.

Donaghay, P. L. and T. R. Osborn (1997). "Toward a theory of biological-physical control of harmful algal bloom dynamics and impacts." Limnology and Oceanography **42**(5): 1283-1296.

Ferreira, J. G., J. H. Andersen, et al. (2011). "Overview of eutrophication indicators to assess environmental status within the European Marine Strategy Framework Directive." Estuarine Coastal and Shelf Science **93**(2): 117-131.

Flindt, M. R., C. B. Pedersen, et al. (2007). "Transport, sloughing and settling rates of estuarine macrophytes: Mechanisms and ecological implications." Continental Shelf Research **27**(8): 1096-1103.

Fonseca, M. S., M. A. R. Koehl, et al. (2007). "Biomechanical factors contributing to self-organization in seagrass landscapes." Journal of Experimental Marine Biology and Ecology **340**(2): 227-246.

Gibson, C. H. (1972). "Turbulent Flow." Science **176**(4034): 503-504.

Grover, J. P., R. W. Sterner, et al. (1999). "Algal growth in warm temperate reservoirs: Nutrient-dependent kinetics of individual taxa and seasonal patterns of dominance." Archiv Fur Hydrobiologie **145**(1): 1-23.

Guedri, H. and C. Durrieu (2008). "A self-assembled monolayers based conductometric algal whole cell biosensor for water monitoring." Microchimica Acta **163**(3-4): 179-184.

Hamilton, G., R. McVinish, et al. (2009). "Bayesian Model Averaging for Harmful Algal Bloom Prediction." Ecological Applications **19**(7): 1805-1814.

Hart, D. D. and C. M. Finelli (1999). "Physical-Biological Coupling in Streams: The Pervasive Effects of Flow on Benthic Organisms." Annual Review of Ecology and Systematics **30**(ArticleType: research-article / Full publication date: 1999 / Copyright © 1999 Annual Reviews): 363-395.

Higgins, S. N., R. E. Hecky, et al. (2008). "The collapse of benthic macroalgal blooms in response to self-shading." Freshwater Biology **53**(12): 2557-2572.

Hondzo, M., T. Feyaerts, et al. (2005). "Universal scaling of dissolved oxygen distribution at the sediment-water interface: A power law." Limnology and Oceanography **50**(5): 1667-1676.

Hondzo, M. and H. Wang (2002). "Effects of turbulence on growth and metabolism of periphyton in a laboratory flume." Water Resour. Res. **38**(12): 1277.

Hui, B. W., G. J. Wen, et al. (2012). "Line-scan camera calibration in close-range photogrammetry." Optical Engineering **51**(5).

Ishino, R. and T. Ishikawa (2001). "Sway measurement of overhead power lines by ITV-based camera." Electrical Engineering in Japan **137**(4): 18-24.

Johnson, M., S. Shivkumar, et al. (1996). "Structure and properties of filamentous green algae." Materials Science and Engineering: B **38**(1–2): 103-108.

Kannel, P. R., S. R. Kanel, et al. (2011). "A Review of Public Domain Water Quality Models for Simulating Dissolved Oxygen in Rivers and Streams." Environmental Modeling & Assessment **16**(2): 183-204.

Khan, Z. H., I. Y. H. Gu, et al. (2011). "A Robust Particle Filter-Based Method for Tracking Single Visual Object Through Complex Scenes Using Dynamical Object Shape and Appearance Similarity." Journal of Signal Processing Systems for Signal Image and Video Technology **65**(1): 63-79.

Kikuchi, H., R. Abe, et al. (2012). "Simple Bitplane Coding and Its Application to Multi-Functional Image Compression." Ieice Transactions on Fundamentals of Electronics Communications and Computer Sciences **E95A**(5): 938-951.

Kim, D. K., K. S. Jeong, et al. (2012). "Machine Learning for Predictive Management: Short and Long term Prediction of Phytoplankton Biomass using Genetic Algorithm Based Recurrent Neural Networks." International Journal of Environmental Research **6**(1): 95-108.

Klein, D. A. and M. W. Paschke (2004). "Filamentous Fungi: The Indeterminate Lifestyle and Microbial Ecology." Microbial Ecology **47**(3): 224-235.

Koehl, M. and A. W. Rosenfeld (2006). Wave-swept shore : the rigors of life on a rocky coast. Berkeley, University of California Press.

Koehl, M. A. R. (1999). "Ecological biomechanics of benthic organisms: Life history mechanical design and temporal patterns of mechanical stress." Journal of Experimental Biology **202**(23): 3469-3476.

Kuhl, M., R. N. Glud, et al. (1996). "Microenvironmental control of photosynthesis and photosynthesis-coupled respiration in an epilithic cyanobacterial biofilm." Journal of Phycology **32**(5): 799-812.

Kuritz, T. and C. P. Wolk (1995). "USE OF FILAMENTOUS CYANOBACTERIA FOR BIODEGRADATION OF ORGANIC POLLUTANTS." Applied and Environmental Microbiology **61**(1): 234-238.

Lan, P. and A. A. Shabana (2010). "Rational Finite Elements and Flexible Body Dynamics." Journal of Vibration and Acoustics-Transactions of the Asme **132**(4).

Larned, S. T., V. I. Nikora, et al. (2004). "Mass-transfer-limited nitrogen and phosphorus uptake by stream periphyton: A conceptual model and experimental evidence." Limnology and Oceanography **49**(6): 1992-2000.

Malavasi, S. and G. Blois (2012). "Wall effects on the flow structure around a rectangular cylinder." Meccanica **47**(4): 805-815.

Malavasi, S. and E. Zappa (2009). "Fluid-dynamic forces and wake frequencies on a tilted rectangular cylinder near a solid wall." Meccanica **44**(1): 91-101.

Martone, P. T. (2007). "Kelp versus coralline: Cellular basis for mechanical strength in the wave-swept seaweed Calliarthron (Corallinaceae, Rhodophyta)." Journal of Phycology **43**(5): 882-891.

Martone, P. T. and M. W. Denny (2008). "To break a coralline: mechanical constraints on the size and survival of a wave-swept seaweed." Journal of Experimental Biology **211**(21): 3433-3441.

Mooi, R. D. and A. C. Gill (2010). "Phylogenies without Synapomorphies-A Crisis in Fish Systematics: Time to Show Some Character." Zootaxa(2450): 26-40.

Nikora, V. (2010). "HYDRODYNAMICS OF AQUATIC ECOSYSTEMS: AN INTERFACE BETWEEN ECOLOGY, BIOMECHANICS AND ENVIRONMENTAL FLUID MECHANICS." River Research and Applications **26**(4): 367-384.

Nikora, V. I., D. G. Goring, et al. (1998). "A Simple Model of Stream Periphyton-Flow Interactions." Oikos **81**(3): 607-611.

Parker, J. E. and S. C. Maberly (2000). "Biological response to lake remediation by phosphate stripping: control of Cladophora." Freshwater Biology **44**(2): 303-309.

Pedersen, M. F., L. B. Nejrup, et al. (2012). "Effects of wave exposure on population structure, demography, biomass and productivity of the kelp Laminaria hyperborea." Marine Ecology-Progress Series **451**: 45-60.

Poff, N. L., N. J. Voelz, et al. (1990). "Algal Colonization under Four Experimentally-Controlled Current Regimes in High Mountain Stream." Journal of the North American Benthological Society **9**(4): 303-318.

Quinn, J., L. de Winter, et al. (2011). "Microalgae bulk growth model with application to industrial scale systems." Bioresource Technology **102**(8): 5083-5092.

Raaijmakers, J. G. W. (1987). "Statistical Analysis of the Michaelis-Menten Equation." Biometrics **43**(4): 793-803.

Rasmussen, E. K., O. S. Petersen, et al. (2009). "Model analyses of the future water quality of the eutrophicated Ghar El Melh lagoon (Northern Tunisia)." Hydrobiologia **622**: 173-193.

Rier, S. T. and R. J. Stevenson (2006). "Response of periphytic algae to gradients in nitrogen and phosphorus in streamside mesocosms." Hydrobiologia **561**: 131-147.

Rubin, H. and J. F. Atkinson (2001). Environmental fluid mechanics. New York, Marcel Dekker.

Ruhnow, F., D. Zwicker, et al. (2011). "Tracking Single Particles and Elongated Filaments with Nanometer Precision." Biophysical journal **100**(11): 2820-2828.

Sanchez, J. L. G., M. Berenguel, et al. (2003). "Minimization of carbon losses in pilot-scale outdoor photobioreactors by model-based predictive control." Biotechnology and Bioengineering **84**(5): 533-543.

Schutten, J. and A. J. Davy (2000). "Predicting the Hydraulic Forces on Submerged Macrophytes from Current Velocity, Biomass and Morphology." Oecologia **123**(4): 445-452.

Steinman, A. D., P. J. Mulholland, et al. (1992). "Functional Responses Associated with Growth Form in Stream Algae." Journal of the North American Benthological Society **11**(2): 229-243.

Su, H. J. (2009). "A Pseudorigid-Body 3R Model for Determining Large Deflection of Cantilever Beams Subject to Tip Loads." Journal of Mechanisms and Robotics-Transactions of the Asme **1**(2).

Thai, H. T. and S. E. Kim (2012). "Second-order inelastic analysis of cable-stayed bridges." Finite Elements in Analysis and Design **53**: 48-55.

Valipour, H. R. and M. Bradford (2012). "An efficient compound-element for potential progressive collapse analysis of steel frames with semi-rigid connections." Finite Elements in Analysis and Design **60**(0): 35-48.

Wallin, A., S. Qvarfordt, et al. (2011). "Benthic communities in relation to wave exposure and spatial positions on sublittoral boulders in the Baltic Sea." Aquatic Biology **12**(2): 119-128.

Westerhoff, P., Q. Hu, et al. (2010). "Growth parameters of microalgae tolerant to high levels of carbon dioxide in batch and continuous-flow photobioreactors." Environmental Technology **31**(5): 523-U580.

Wullepit, N., M. Hostens, et al. (2012). "Influence of a marine algae supplementation on the oxidative status of plasma in dairy cows during the periparturient period." Preventive Veterinary Medicine **103**(4): 298-303.

Xu, J. P., L. D. Wright, et al. (1994). "Estimation of Bottom Stress and Roughness in Lower Chesapeake Bay by the Inertial Dissipation Method." Journal of Coastal Research **10**(2): 329-338.

Young, D. F. (2007). A brief introduction to fluid mechanics. Hoboken, NJ, Wiley.